International Journal of Heat and Mass Transfer 224 (2024) 125297

Contents lists available at ScienceDirect

International Journal of Heat and Mass Transfer

journal homepage: www.elsevier.com/locate/ijhmt

Assessment and development of saturated and subcooled heat transfer coefficient correlations for cryogenic flow boiling in tubes

Sunjae Kim [a], Steven J Darges [a], Jason Hartwig [b], Issam Mudawar [a,1,*]

[a] Purdue University Boiling and Two-Phase Flow Laboratory (PU-BTPFL), School of Mechanical Engineering, Purdue University, 585 Purdue Mall, West Lafayette, IN 47907, USA
[b] Fluids and Cryogenics Branch, NASA Glenn Research Center, 21000 Brookpark Rd, Cleveland, OH 44135, USA

ARTICLE INFO

Keywords:
Cryogenic flow boiling
Saturated boiling
Subcooled boiling
Two-phase heat transfer coefficient
Universal correlations
Gravity effect

ABSTRACT

The escalating interest in cryogenic technologies for space-related applications has led to an unprecedented demand for reliable prediction methods for cryogenic two-phase flow and heat transfer. Regrettably, existing heat transfer coefficient (HTC) correlations developed for conventional fluids prove inadequate and provide subpar predictions when applied to cryogenic flow boiling conditions. Therefore, it is imperative to develop a set of new HTC correlations specifically tailored for cryogenic flow boiling. In this study, comprehensive databases are constructed consolidating experimental data from previous studies of the present authors and historical data extracted from open literatures, spanning a wide range of operating conditions, flow orientations, and various cryogenic fluids. Subsequently, based on the constructed databases, an assessment of the predictive accuracy of seminal HTC correlations is conducted, followed by the development of new HTC correlations for cryogenic saturated and subcooled flow boiling. The newly developed correlations demonstrate very good predictive accuracy, with an overall mean absolute error (MAE) of 23.84 % and 21.24 % for LN_2 saturated and subcooled HTC, respectively, under terrestrial gravity conditions. When assessed against a microgravity dataset, these correlations exhibit equally good predictive accuracy, yielding MAE values of 16.73 % and 25.99 % for LN_2 saturated and subcooled HTC, respectively. Furthermore, the universal applicability of the new HTC correlations is ascertained by assessing the correlations across a multitude of cryogenic fluids, including LN_2, LHe, LAr, LCH_4, and LH_2. Impressively, these correlations display outstanding predictive accuracy, with MAE values of 24.01 % and 21.29 % for saturated and subcooled HTC, respectively, underscoring their superior performance across a wide range of cryogenic fluids, validated against 2,445 saturated cryogenic HTC datapoints and 1,553 subcooled cryogenic HTC datapoints. Overall, the new HTC correlations consistently outperform all prior seminal correlations, yielding good predictive accuracy across a diverse spectrum of operating conditions, irrespective of flow orientation and gravity level, for various cryogenic fluids.

1. Introduction

1.1. Two-phase flow and heat transfer physics for space thermal management systems

As the global space race continues, achieving aerospace technological superiority has become a common goal worldwide. Among the desired aerospace technologies, the implementation of two-phase thermal management systems [1,2] is of great interest to various space agencies worldwide, including NASA, due to their potential to offer energy-efficient and compact cooling solutions for high-power-density applications where conventional single-phase thermal management schemes are inadequate. In response to the spiking demand for high performance thermal management technologies, many of thermal researchers and engineers developed innovative two-phase cooling techniques, including hybrid-cooling [3,4], bidirectional counter-flow heat sinks [5] and manifold micro-channel heat sinks [6,7], let alone conventional techniques: pool boiling [8,9], spray [10–14] and jet impinging [15–18], and mini/micro-channel heat sinks [19,20]. Among these techniques, recent endeavors from researchers has been focused on advancing the flow boiling schemes. Key to their adaptability are small weight and volume requirements (often using “cold plates’) and ability to tackle high-heat-fluxes, the latter being outcome of reliance on fluid

* Corresponding author.
E-mail address: mudawar@ecn.purdue.edu (I. Mudawar).
[1] website: http://engineering.purdue.edu/BTPFL

https://doi.org/10.1016/j.ijheatmasstransfer.2024.125297
Received 31 October 2023; Received in revised form 12 January 2024; Accepted 6 February 2024
Available online 16 February 2024

Nomenclature

A	area (m^2)
a	Schrage et al.'s functional parameter, $w_0/(2\bar{R}T/\bar{M})^2$
Bo	boiling number, q''/Gh_{fg}
Co	confinement number, $\sqrt{\sigma/((\rho_f-\rho_g)gD^2)}$
$c_{p,f}$	specific heat of liquid
D	diameter (mm)
F	enhancement factor
F_f	empirical constant incorporated in Fang et al.'s correlation
$Fr_{fo,D}$	liquid-only Froude number based on tube diameter, $G^2/\rho_f gD$
Fr_{fo}^{**}	modified liquid-only Froude number, $(G+800)^2/\rho_f^2(g_e-g)D$
f_{sp}	Fanning friction factor corresponding to single phase flow
G	mass velocity (kg/m^2s)
g	gravitational acceleration (m/s^2); specific Gibbs free energy (J/kg)
g_e	Earth gravity (m/s^2)
h	enthalpy (J/kg); heat transfer coefficient (kW/m^2K)
h_{fg}	latent heat of vaporization (J/kg)
J	rate of bubble nucleation per unit volume per unit time
Ja	Jacob number, $c_{p,f}\Delta T_{sat}/h_{fg}$
Ja^{**}	modified Jacob number, $c_{p,f}\Delta T_{sub}/h_{fg}$
j_{nc}	number of molecules condensing into interface per unit area per unit time
j_{ne}	number of molecules evaporating from interface per unit area per unit time
k	thermal conductivity (W/m•K)
k_B	Boltzmann constant (1.380649×10^{-23} m^2kg/s^2•K)
L	length (m)
La	Laplace length, $\sqrt{\sigma/(\rho g)}$
L_b	bubble length scale, $\sqrt{\sigma/((\rho_f-\rho_g)g)}$
L_e	entrance length (mm)
L_H	heated length (mm)
$\bar{M}$	molecular weight
m	mass of a single molecule (kg)
N	number of datapoints
n	size of vapor embryo; number of molecules
N_f	number distribution of liquid molecules per unit volume
N_n	number distribution of vapor embryos with size n per unit volume
P	pressure (Pa)
P_R	pressure ratio, P/P_{crit}
Pr	Prandtl number
q''	wall heat flux (W/m^2)
$\bar{R}$	ideal gas constant (≈ 8.314 J/Kmol)
R_b	bubble radius (m)
Re_f	liquid Reynolds number, $GD(1-x_e)/\mu_f$
Re_{fo}	liquid-only Reynolds number, GD/μ_f
S	suppression factor, entropy
T	temperature (°C, K)
ΔT_{sub}	fluid subcooling, T_{sat} - T_f
Th	wall thickness (mm)
U	internal energy (J/kg)
u	x-component of velocity vector (m/s)
V	volume (m^3)
v	y-component of velocity vector (m/s)
w	z-component of velocity vector (m/s)
We	Weber number, $G^2D/(\rho_f\sigma)$
x_e	thermodynamic equilibrium quality
X_{tt}	Lockhart-Martinelli parameter, $\left(\frac{1-x_e}{x_e}\right)^{0.9}\left(\frac{\rho_f}{\rho_g}\right)^{0.5}\left(\frac{\mu_f}{\mu_g}\right)^{0.1}$
z	axial coordinate (m)
$\Delta z_{sat}/L_H$	saturation length ratio, defined in Eq. (10)

Greek symbols

α	void fraction
Γ	effect of bulk motion, defined in Eq. (A28)
θ	flow orientation angle; contact angle
μ	dynamic viscosity (kg/m•s)
ν	kinematic viscosity (m^2/s)
ρ	density (kg/m^3)
σ	surface tension (N/m)
Ψ	availability, defined in Eq. (A1)

Subscripts

b	bubble
CB	convective boiling
$crit$	critical
f	liquid
fo	liquid-only
g	vapor
i	inner tube wall, interface
in	inlet to heated tube
$meas$	measured
NB	nucleate boiling
o	outer tube wall
out	outlet
PB	pool boiling
$pred$	predicted
s	sold wall
sat	saturation
sp	single phase
sc	subcooling
tp	two phase
w	wall
z	local

Acronyms

CFM	cryogenic fluid management
CHF	critical heat flux
FDB	fully developed boiling
HTC	heat transfer coefficient
HV	hand (ball) valve
LAr	liquid argon
LCH_4	liquid methane
LH_2	liquid hydrogen
LHe	liquid helium
LN_2	liquid nitrogen
LNe	liquid neon
MAE	mean absolute error
NTP	nuclear thermal propulsion
ONB	onset of nucleate boiling
PDB	partially developed boiling
PWR	pressurized water reactor
SV	solenoid valve

motion rather than body force to flush bubbles away from and sustain supply of bulk liquid to heated surfaces. Supporting the statement, a recently published NASA technical report [21] cited flow boiling systems as vital for safe operation of onboard life support systems, avionics, Rankine power systems, and high-power-density energy conversion equipment.

1.2. Cryogenic flow boiling for space applications

Due to the notably high performance in terms of specific impulse and energy density compared to conventional propellants, cryogenic propellants have garnered significant attention in recent years, particularly for space exploration. Moreover, a recently reported NASA roadmap [22] designated cryogenic fluid management (CFM) technologies as a key to successful future space exploration missions. Two main space systems that capitalize on the CFM technology the most are cryogenic fuel depots and Nuclear Thermal Propulsion (NTP) powered vehicles. These systems typically involve the transfer of cryogenic liquids from a large volume storage tank to smaller tanks or spacecraft [23]. During the fuel transfer, it is crucial to ensure that the system hardware, including the feed line, flow components, and various storage tanks, be cooled down to cryogenic temperatures before providing vapor-free liquid. The cooling process is typically achieved through phase change heat transfer, where a portion of the propellant is allowed to boil, effectively removing thermal energy from the system walls [24], which highlights the importance of understanding flow boiling fluid physics of cryogens. Furthermore, NTP, whether designed to provide the thrust to move a spacecraft between orbits or operate as a dual-mode system that provides power and propulsion capability, provides strong architectural benefits to exploration missions and reusable in-space transportation systems [25]. Such NTP systems use a nuclear reactor to heat a propellant, such as LH_2, which is then expelled out of a nozzle to produce thrust and also be used as coolant for maintaining acceptable temperature of the nuclear reactor. Consequently, the importance of understanding cryogenic two-phase fluid physics and flow boiling should be highlighted in order to design high fidelity NTP and incorporated feed systems of NTP; this is equivalent to how thermal hydraulic understanding of water is crucial for pressurized water reactors (PWRs) in Earth-based nuclear reactors. Additional applications where CFM technologies play a critical role include, but are not limited to, ascent and descent stages, feedlines for gas/gas or liquid/liquid engines, and superconducting hydrogen aircraft. Fig. 1 shows examples of in-space applications requiring CFM technology.

While the utilization and implementation of cryogenic two-phase systems hold significant importance for space applications, a key challenge lies in accurately predicting the performance of cryogenic two-phase flow and heat transfer under various gravitational environments. Cryogenic fluids, in comparison to conventional fluids, exhibit unique and extreme thermal properties, leading to distinct fluid physics and energy transport phenomena during flow boiling. Accordingly, existing HTC correlations based on room temperature fluids are inadequate for predicting heat transfer for cryogens. Specifically, existing correlations have been found to overpredict LH_2 quenching heat transfer data by as much as 200 percent [24], and significant disparities between correlations for conventional fluids and cryogenic flow boiling data in heated tubes have also been reported [26]. The absence of reliable design tools poses a substantial obstacle in the development of secure and reliable CFM systems. Consequently, it becomes imperative to develop robust and reliable predictive design tools specifically tailored for cryogenic flow boiling. Such tools are essential to ensure the safety and effectiveness of CFM systems, especially under the unprecedented demands for cryogenic space applications.

1.3. Subcooled and saturated flow boiling

1.3.1. Subcooled flow boiling

In two-phase thermal management applications, the conventional practice is to supply subcooled liquid coolants into fluid channels. This strategy maximizes cooling efficiency by utilizing both the sensible heat and latent heat of the subcooled liquid coolant. However, subcooled flow boiling typically leads to significant thermal non-equilibrium, characterized by variations in temperature and void fraction across the flow area. This gradual thermal non-equilibrium gives rise to two distinct regimes in subcooled boiling: partially developed boiling (PDB) and fully developed boiling (FDB). As depicted in Fig. 2, once the onset of nucleate boiling (ONB) is exceeded, PDB commences, accompanied by a slight but measurable rise in void fraction. During the PDB regime, nucleated bubbles adhere to the heated wall, primarily because of the substantial effect of bulk condensation. This effect restricts any substantial escalation in void fraction. The transition to the FDB regime is marked by the departure of the first bubble from the heated surface, after which it migrates toward the bulk fluid. During the FDB regime, nucleated bubbles effectively carry heat energy away from the heated surface as they detach and move into the bulk fluid, leading to an increase in the bulk fluid temperature. Consequently, with weaker condensation occurring in the now warmer bulk fluid, the void fraction increases more rapidly along the channel. Once the thermodynamic equilibrium quality, x_e, reaches zero, subcooled boiling ceases, and the flow boiling regime shifts into saturated flow boiling. It can be inferred from this straightforward analysis that the heat transfer physics of subcooled boiling will be primarily influenced by bubble nucleation and bubble dynamics. This is more likely the case for cryogens, as introduced in Ganesan et al. [27], where nucleate boiling was shown to commence at lower surface superheat and eventually leading to a larger number of small bubbles forming at and ultimately departing from the surface due to low surface tension and low latent heat of vaporization.

Associated heat transfer characteristics for subcooled boiling have been studied for decades and various subcooled HTC correlations were proposed, which can be broadly categorized into three different groups: (i) correlations based on dimensionless group analysis (e.g., Papell [28], Badiuzzaman [29], Hodgson [30], Moles and Shaw [31], Shaw [32], Devahdhanush and Mudawar [33]), (ii) correlations based on superposition of single-phase convection and nucleate boiling heat transfer correlations (e.g., Bjorg et al. [34], Gungor and Winterton [35], Liu and Winterton [36]), and (iii) correlations that have characteristics of the other types and have intermediate forms (e.g., Shah [37,38]). Representative seminal correlations [28,31,33,36,38] for subcooled flow boiling heat transfer coefficient are selected and assessed in this study. Note that the selected correlations are derived from consolidated databases that cover a minimum of two substantially different fluids, except for the HTC correlation by Devahdhanush and Mudawar [33] which was developed based only on n-perfluorohexane (n-PFH) but has a superior functional form to avoid the numerical divergence issue of the dimensionless group-type correlations. The numerical divergence issue will further be discussed in a later section.

1.3.2. Saturated flow boiling

Saturated flow boiling commences when the thermodynamic equilibrium quality, x_e, exceeds zero, as illustrated in Fig. 2. In saturated flow boiling, two distinct heat transfer regimes have been identified based on mechanisms that dominate the largest fraction of channel length upstream of the critical heat flux (CHF) location. Fig. 3(a) illustrates Nucleate Boiling Dominant heat transfer, characterized by a significant portion of the channel length being occupied by bubbly and slug flow. During this regime, the heat transfer coefficient exhibits a monotonically decreasing trend due to the gradual suppression of nucleate boiling. Fig. 3(b) displays the second regime, known as Convective Boiling Dominant heat transfer, where a substantial section of the channel is dominated by annular flow. Within this regime, the heat transfer

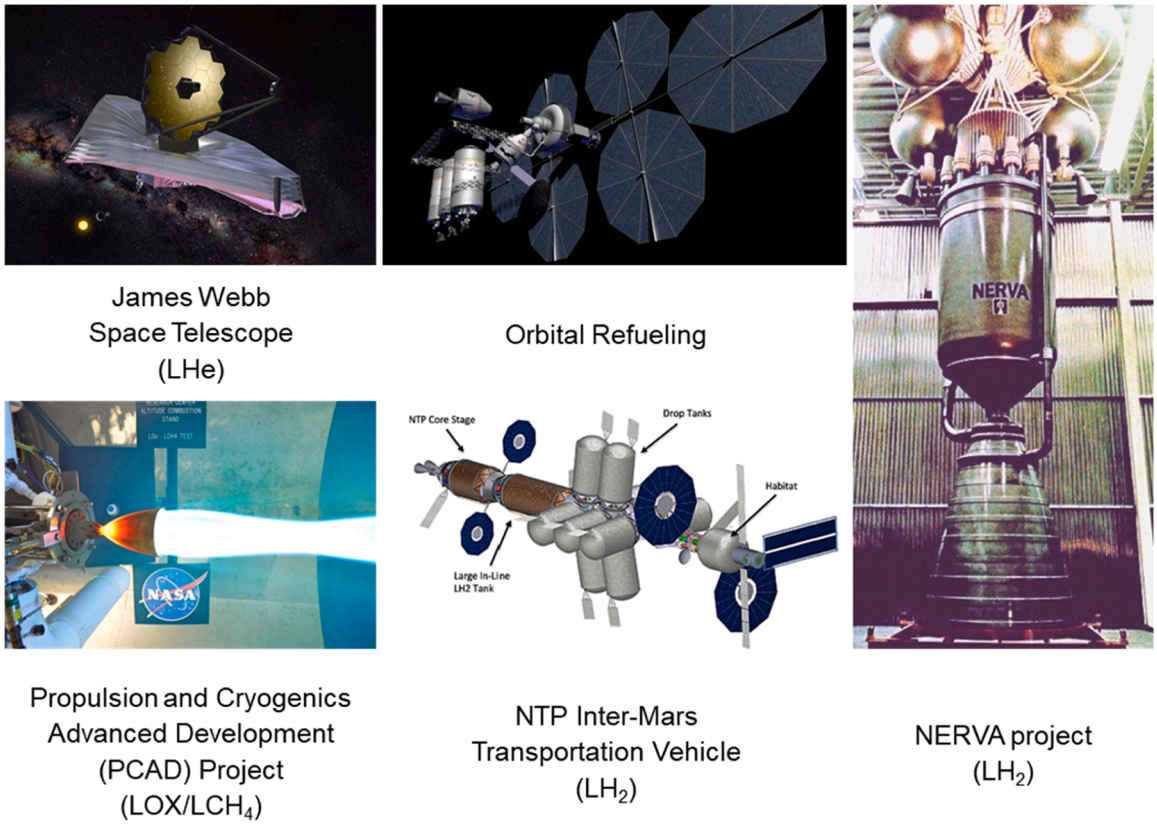

Fig. 1. Space applications of cryogens.

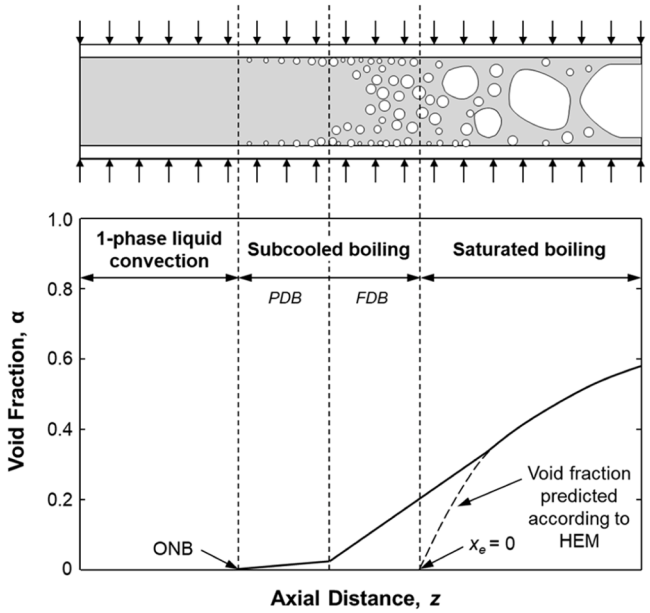

Fig. 2. Void fraction variations associated with partially developed boiling (PDB) and fully developed boiling (FDB) sub-regions of subcooled boiling, and with saturated boiling.

coefficient demonstrates an increasing trend along the channel length due to the gradual thinning of the annular liquid film.

Hence, it is evident from the above observations that the nucleate boiling and convective boiling mechanisms contribute the most heat transfer to the bubbly and annular flow regimes, respectively, with intermediate flow regimes having partial contributions of both mechanisms. These insights have served as a foundation for formulating the superposition functional relation for the saturated flow boiling HTC, h_{tp}, as

$$h_{tp}^{\ n} = [h_{NB}]^n + [h_{CB}]^n \quad (1)$$

Various saturated HTC correlations have been reported historically which can be broadly categorized into two main groups based on the functional formulation of h_{NB}: (i) h_{NB} depending on pool boiling HTC, h_{PB}, supplemented with the *suppression factor, S* (e.g., Chen [39], Klimenko [40], Liu and Winterton [36], Steiner and Taborek [41]), and (ii) h_{NB} represented by a single-phase liquid HTC, $h_{sp,f}$, supported with combination of *Bo, Pr*, and (1-x_e) (e.g., Schrock and Grossman [42], Shah [43], Gungor and Winterton [35], Kim and Mudawar [44], Ganesan et al. [27]). Representative seminal correlations [27,35,36,39–41,43,44] for saturated flow boiling heat transfer coefficient are selected and assessed in this study.

1.4. Objectives of present study and strategy for developing the new correlations

Since 2020, a primary objective of the Purdue University Boiling and Two-Phase Flow Laboratory (PU-BTPFL) has been to establish a comprehensive experimental database for cryogenic flow boiling, encompassing various gravity levels and flow orientations utilizing liquid nitrogen (LN_2) as the working fluid. Over the course of recent years, a number of LN_2 flow boiling experiments have been meticulously conducted, yielding a substantial dataset for diverse flow orientations under Earth gravity [45,46] and microgravity [47]. While the prior work has exhaustively examined the underlying flow boiling physics, the pursuit of predictive analysis pertaining to flow boiling heat transfer coefficients remains unexplored. This study is designed with the following objectives: (i) aggregation of datapoints encompassing subcooled and saturated flow boiling heat transfer coefficients, spanning a

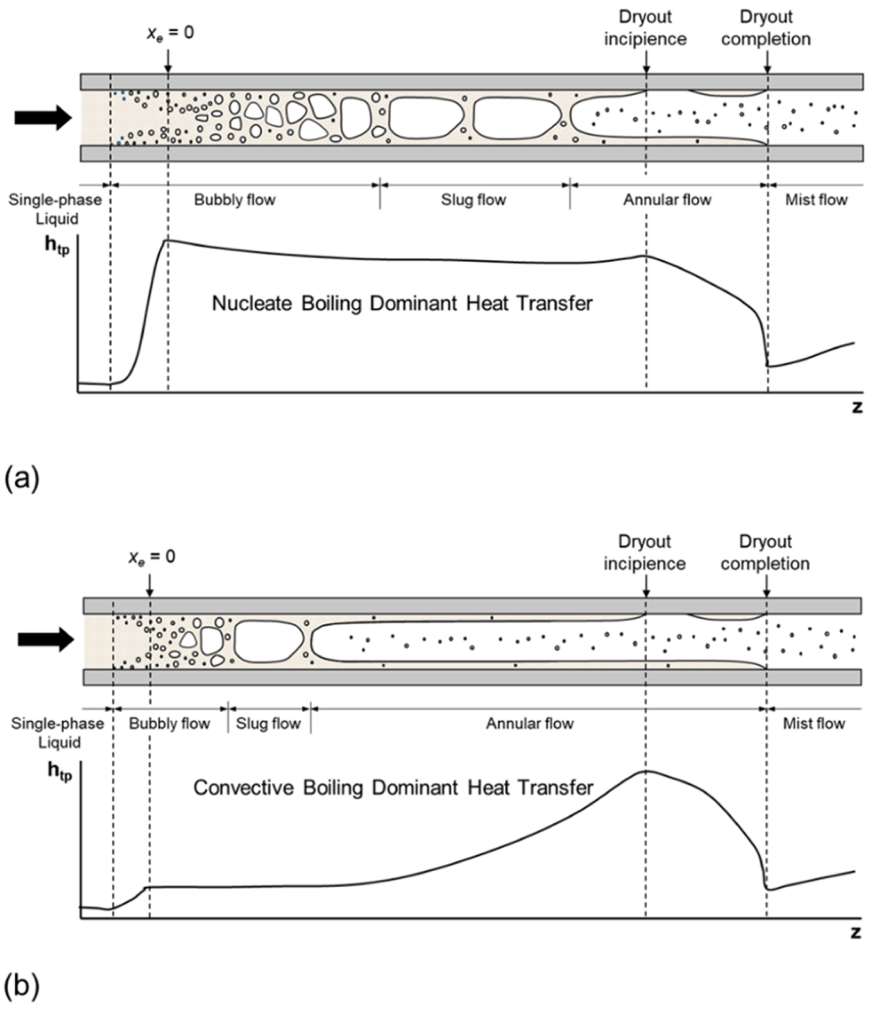

Fig. 3. Schematics of variation in heat transfer coefficient along uniformly heated channel for (a) Nucleate Boiling Dominant heat transfer and (b) Convective Boiling Dominant heat transfer.

wide spectrum of operational parameters, flow orientations, and gravity levels; (ii) assessment of the predictive capabilities of existing HTC correlations using the consolidated database; (iii) development of new correlations for saturated and subcooled heat transfer coefficients that exhibit effectiveness across all flow orientations and gravity levels; and (iv) extensive application of the new correlation for various cryogens in pursuit of universality.

In the systematic pursuit of the aforementioned objectives, a methodical approach was employed. First, HTC datapoints were consolidated and categorized into saturated and subcooled HTC datasets. Each dataset comprises experimental data derived from the studies of the present authors and historical data extracted from open literatures. Subsequently, these assembled datasets were refined by applying various segregation criteria to better align with the demands of cryogenic space applications, as illustrated in Fig. 1. Second, existing seminal correlations were evaluated against the compiled database, with an in-depth discussion of each correlation's characteristics. Third, new HTC correlations were formulated and rigorously tested for their accuracy using datasets of both terrestrial gravity and microgravity conditions. Furthermore, these newly developed HTC correlations were validated for their universal applicability by testing them with various cryogenic fluids, not only LN_2. This comprehensive methodology was systematically executed for both saturated and subcooled HTC correlations.

2. Experimental methods and database

2.1. Experiment facility

The present study utilizes HTC data derived from recent experimental investigations conducted by the present authors. Therefore, only a brief overview of the experimental methods is discussed herein to facilitate comprehension of the obtained outcomes. For further details on the different components, instrumentation, measurement uncertainties, operating procedure, imaging technique, and more, the reader is encouraged to consult the original publications where these experiments were initially documented. This includes 1-g_e horizontal LN_2 flow boiling experiments [45], microgravity LN_2 flow boiling experiments conducted using parabolic flights [47], and 1-g_e multiple flow orientation LN_2 flow boiling experiments [46], covering vertical upward, vertical downward, 45° inclined upward, and 45° inclined downward orientations. Table 1 summarizes the key parameters of all local subcooled and saturated flow boiling datapoints for each subset of the experimental database.

2.1.1. Two-phase flow loop

Fig. 4 illustrates a schematic of the open-loop two-phase flow system utilized to (i) provide working fluid, LN_2, into the test section and (ii) safely vent fluid from the test section outlet to ambient air. Since the loop is designed as an open circuit, a nitrogen gas cylinder is connected to the LN_2 dewar to provide positive ullage pressure and displace the

Table 1
Summary of key parameters of the cryogenic flow boiling database using LN_2.

Cryogenic Flow Boiling Experiment Database (LN_2)						
Reference	Vertical Up	Vertical Down	Horizontal	45° Up	45° Down	Microgravity
Number of datapoints, N	1098	843	1134	726	363	249
Mass flow rate, $\dot{m}$ [kg/s]	0.02 – 0.05	0.03 – 0.07	0.02 – 0.09	0.02 – 0.06	0.02 – 0.05	0.02 – 0.07
Mass velocity, G [kg/m^{2}s]	396.35 – 937.73	462.28 – 1154.70	406.76 – 1572.77	351.80 – 1100.66	420.76 – 941.68	362.13 – 1342.86
Pressure, P [kPa]	389.9 – 1032.97	371.52 – 690.74	297.14 – 498.55	368.76 – 887.62	379.48 – 554.51	399.04 – 737.31
Inlet subcooling, ΔT_{sc} [K]	0.1 – 3.7	1.0 – 4.3	0.6 – 4.4	0.1 – 3.2	0.6 – 3.3	1.0 – 5.7
Saturation temperature, T_{sat} [K]	90.9 – 104.3	90.4 – 98.3	87.8 – 94.0	90.3 – 101.9	90.6 – 95.3	91.2 – 99.2
Quality, x_e	−0.05 – 0.28	−0.05 – 0.24	−0.05 – 0.19	−0.04 – 0.23	−0.04 – 0.22	−0.07 – 0.12
Heat flux, q'' [kW/m^2]	1.39 – 103.95	2.46 – 104.29	1.60 – 105.97	2.74 – 108.56	2.72 – 101.85	2.76 – 100.37

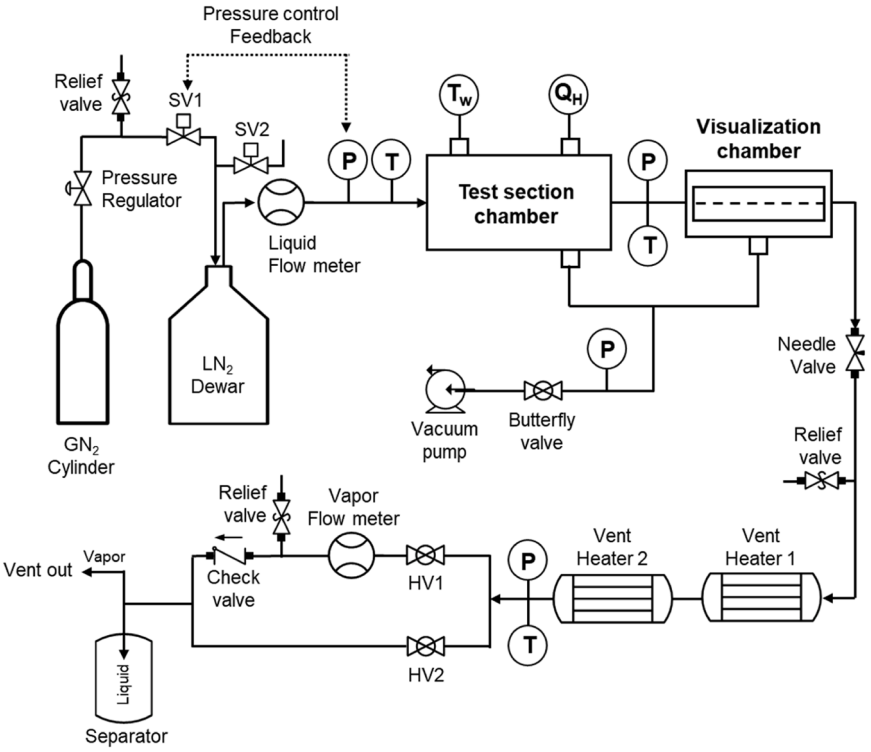

Fig. 4. Schematic of two-phase flow loop.

LN_2 from the dewar. A turbine flow meter is employed to measure the volume flow rate of the liquid. For accurate determination of the mass flow rate, fluid density information is necessary. To obtain precise thermal property values for the incoming liquid, the temperature and pressure of the fluid are measured immediately downstream from the flow meter. The liquid then enters the test section, where a finite amount of heat is added, causing the fluid to undergo phase change and emerge as a two-phase mixture. At the outlet of the test section, fluid temperature and pressure are measured at the same axial location. The fluid is then directed into an adiabatic visualization chamber utilizing a transparent Pyrex tube, which permits interfacial behavior to be captured with the aid of a high-speed video camera (additional design details relating to the test section and visualization chamber are provided in the next section). To regulate the flow rate, a cryogenic grade needle valve is installed downstream of the visualization section. Two 3-kW rated vent heaters are serially connected downstream of the needle valve to completely evaporate any remaining two-phase mixture to pure vapor phase. At the outlet of the second vent heater, fluid temperature and pressure are measured, which, coupled with the volume flow rate reading from a vapor flow meter, facilitate determination of the mass flow rate. The flow loop is divided into two separate flowlines: one includes the vapor flow meter, and the other does not. The flow into these parallel flowlines is manually controlled using ball valves, as indicated in Fig. 4, labeled HV1 and HV2. The vapor flow meter is used to measure low fluid mass velocities below 100 kg/m^{2}s while mass velocities above 100 kg/m^{2}s are measured by the upstream liquid flow meter. However, mass velocity range for the present study never reached below 100 kg/m^{2}s. Further downstream, the two flowlines are combined and connected to a receiver tank which serves to eliminate any possibility of liquid escaping outboard in improbable situations such as vent heater power loss. Finally, during ground testing, the vapor is safely discharged through a vent hose to the ambient environment.

2.1.2. Heat transfer test section and visualization section

The primary components of the payload are the test section and the visualization section. The test section is comprised of a heated tube that is enclosed within a vacuum chamber serving to minimize heat loss. As shown in Fig. 5(a), the vacuum chamber has an inner diameter (i.d.) of 0.1 m and length of 0.8 m and is fitted with flanges on both ends to ensure vacuum tight enclosure. A center hole is machined through each flange for insertion of the heated test section. The vacuum chamber is equipped with four feedthrough ports, three are vertical and one horizontal. The two vertical feedthroughs near to the outlet are for vacuum hose connections while the foremost vertical feedthrough passes wires

from the thermocouples attached to the outer wall of the test section to an external control box containing the data logger. The horizontal feedthrough passes heater power leads from the test section's eight individual heaters. The test section assembly is comprised of a heating tube, eight individual heaters, and thermocouples wires. The test section heated tube is a thin walled ($Th = 0.5$ mm) stainless steel (SS304) tube with i.d. of $D_i = 8.5$ mm, heated length $L_H = 0.68$ m, and entrance length $L_e = 0.112$ m. Eight individual electrically powered coil heaters, depicted schematically in Fig. 5(a), surround the test section's heated tube to provide uniform heat flux along the tube wall. At 120 VAC power input, each heater can dissipate up to 400 W, for a total capacity for the eight heaters of up to 3200 W. Seven pairs of thermocouples are attached to the heated tube wall at seven axial locations, one in each pair is mounted at the top and a second at the bottom. Detailed axial locations of the thermocouples are provided in table form in 5(a). Aside from using vacuum to minimize heat loss, the entire test section assembly is wrapped with layers of insulation which are covered with aluminum sheet to minimize loss by radiation.

Shown schematically in Fig. 5(b), the visualization section is comprised of an adiabatic glass tube enclosed in a visualization vacuum chamber. The tube is made of Pyrex glass and fitted on one end with flexible metal bellows to accommodate thermal expansion as captured in Fig. 5(b). The adiabatic glass tube has outer diameter of $D_o = 9.5$ mm and length of 364.2 mm. The vacuum chamber, which is intended to minimize heat transfer to the glass tube, features rectangular stainless-steel construction with inlet and outlet flanges on both ends to ensure tight vacuum enclosure. As shown in Fig. 5(b), transparent glass windows are attached to opposite lateral sides providing a visualization length of 0.25 m; one window is used for video camera viewing and the other for backlight illumination.

2.2. Data processing

Steady state data are extracted from recorded temporal data by identifying each heater increment and confirming wall temperature reaching steady state. Extracted temporal data are averaged for each steady state period. Necessary thermophysical properties for nitrogen are retrieved from NIST-REFPROP [48].

Test section inlet enthalpy is found based on measured inlet temperature, T_{in}, and inlet and pressure, P_{in}, as

$$h_{in} = h(T_{in}, P_{in}) \tag{2}$$

Test section local enthalpy, h, at any z location from the heated inlet, and outlet enthalpy, h_{out}, are both calculated by application of energy conservation,

$$h(z) = h_{in} + \frac{q'' \pi D_i z}{G\left(\pi D_i^2/4\right)} \tag{3a}$$

$$h_{out} = h_{in} + \frac{q'' \pi D_i L_H}{G\left(\pi D_i^2/4\right)} \tag{3b}$$

Local thermodynamic equilibrium quality, $x_{e,z}$, is calculated according to the relation

$$x_{e,z} = \frac{h - h_f\big|_P}{h_{fg}\big|_P} \tag{4}$$

where h_f, and h_{fg} are, respectively, saturated liquid enthalpy, and latent heat of vaporization corresponding to local pressure which is linearly interpolated between measured inlet pressure, P_{in} and outlet pressure, P_{out}.

Local fluid temperature is determined based on the following relations:

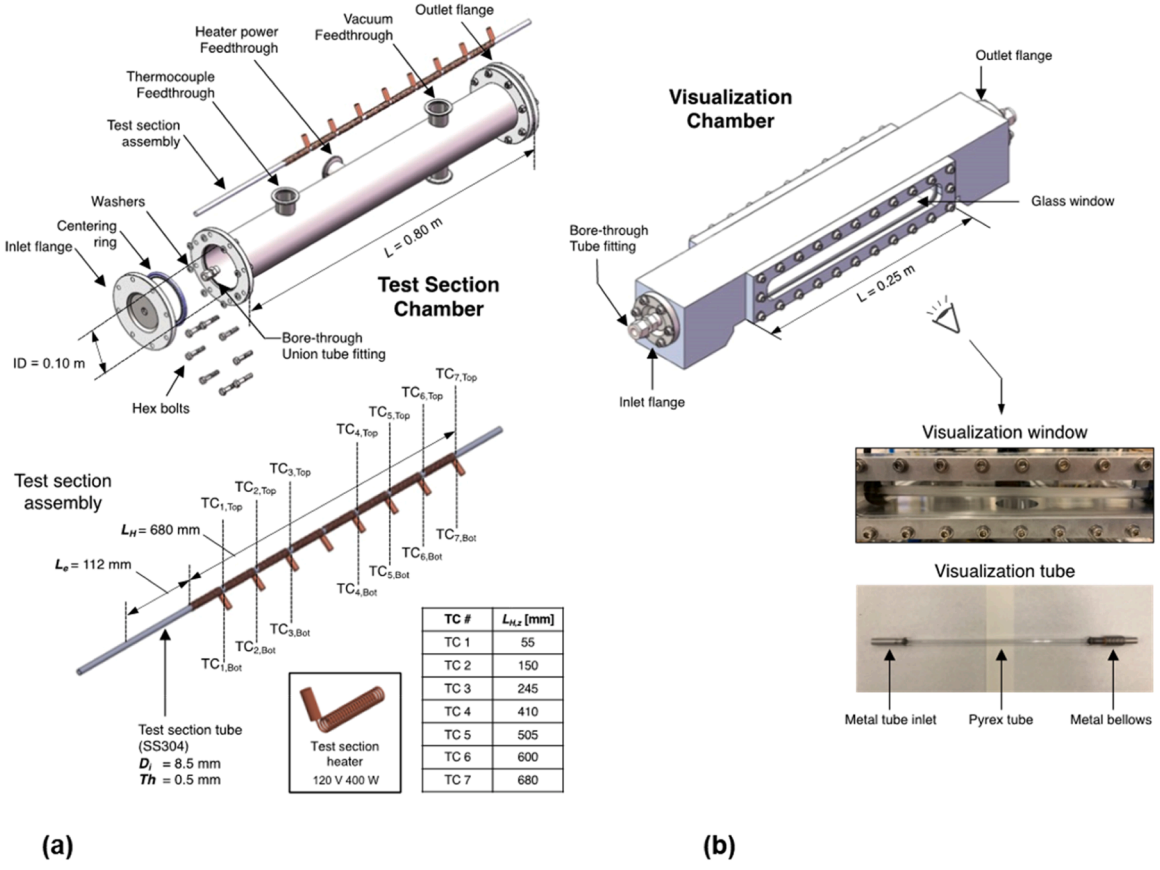

Fig. 5. Schematics of (a) test section chamber and assembly, and (b) visualization chamber with pictures of visualization window and Pyrex tube.

$$T_{f,z} = \begin{cases} T_{in} + \left(T_{sat}|_{xe=0} - T_{in}\right)\dfrac{Z}{L_{sp}} & x_{e,z} < 0 \\ T_{sat,z} & 0 \le x_{e,z} \le 1 \end{cases} \quad (5)$$

where L_{sp} is the heated single-phase length, which is calculated as

$$L_{sp} = \frac{G\left(\pi D_i^2/4\right)}{q''\pi D_i}\left(h_f|_{P_{in}} - h_{in}\right) \quad (6)$$

The local heat transfer coefficient (HTC) is defined based on measured local wall temperature and calculated local fluid temperature for each axial location,

$$h_z = \frac{q''}{\left(T_{w,z} - T_{f,z}\right)} \quad (7)$$

Local inner wall temperature, $T_{w,z}$, at each axial thermocouple location is determined from measured outer wall temperature, $T_{w,o,z}$, and measured heat flux, q'', by accounting for conduction resistance across the heated tube wall,

$$T_{w,z} = T_{w,o,z} - \frac{q''\pi D_i \ln(D_o/D_i)}{2\pi k_s} \quad (8)$$

The average HTC is calculated using the relation

$$\bar{h} = \frac{\iint dA}{\iint \frac{1}{h_z} dA} \quad (9)$$

which is based on harmonic averaging as proven by Ganesan et al. [27] for a constant wall heat flux boundary.

2.3. Experimental cases and historical database

2.3.1. Experimental cases

The experimental database as summarized in Table 1 includes both saturated and subcooled datapoints for LN_2 flow boiling. Thus, the imperative arises to segregate these datapoints into two distinct categories: one for saturated conditions and the other for subcooled conditions. This segregation is judiciously executed based on the thermodynamic equilibrium quality, as visually depicted in Fig. 6. In Fig. 6, a total of 4152 1-g_e HTC datapoints for vertical upward, vertical downward, horizontal, 45° inclined upward, 45° inclined downward are exhibited. The broken vertical line indicates zero thermodynamic equilibrium quality, $x_e = 0$, and classifies those on the right-hand side of the line as saturated HTC datapoints and those on the left-hand side as a mixture comprising single-phase liquid and subcooled HTC datapoints. Consequently, this delineation yields a total of 2080 HTC datapoints classified as the saturated HTC dataset, while 2072 datapoints are allocated to the mixture of single-phase liquid and subcooled HTC dataset. Note that the mixture of single-phase liquid and subcooled HTC dataset will further be segregated in later sections using ONB criteria.

2.3.2. Historical database

Other saturated HTC and subcooled HTC datapoints are extracted from a diverse array of references, including (1) cryogenic journals, (2) cryogenic conferences, (3) technical reports from NASA and NIST, and (4) various sporadic publications, reports, and theses from around the world. The extracted HTC datapoints were consolidated and segregated into a saturated historical database and a subcooled historical database. The saturated historical database was deliberately introduced and analyzed by Ganesan et al. [27]. However, in contrast to the extensive body of literature available for cryogenic saturated HTC, the scarcity of cryogenic subcooled HTC literature warrants special attention. Nonetheless, the available subcooled HTC datapoints were meticulously compiled from a limited number of references [49–55]. Of those, hydrogen data from Core et al. [49] has been deliberately excluded from the subcooled historical database due to the original authors' observations of abnormally high scatter of the data attributed to experimental uncertainties and two-phase flow instabilities during the experiments.

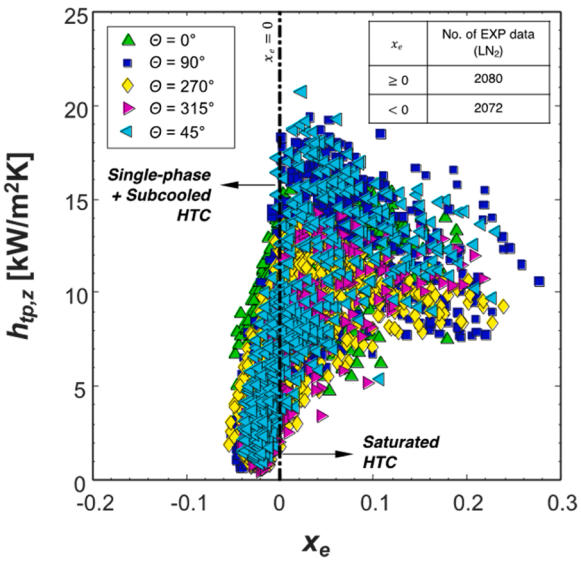

Fig. 6. Distinguishing experimentally measured data into saturated and subcooled heat transfer coefficients based on equilibrium quality.

Table 2 provides an overview of the consolidated LN_2 database, encompassing both experimental and historical HTC datasets. The forthcoming assessments of seminal correlations and the development of the new HTC correlations in the subsequent sections will primarily be built upon this consolidated LN_2 database. Subsequently, the remaining HTC datapoints for other cryogenic fluids from the historical dataset will be harnessed to examine the universal applicability of the newly devised HTC correlations, as suggested in Section 1.3.

3. Saturated heat transfer coefficient

3.1. Data demarcation and trends

The saturation length ratio, $\Delta z_{sat}/L_H$, has been proposed by Ganesan et al. [27] and is defined as

$$\frac{\Delta z_{sat}}{L_H} = \frac{x_e}{4Bo}\left(\frac{D}{L_H}\right) \quad (10)$$

This parameter serves as a quantifiable indicator of the two-phase mixture's inlet quality, facilitating the segregation of saturated HTC datapoints into two distinct categories: low vapor content points and high vapor content points. This categorization holds significant importance as it plays a pivotal role in determining HTC, given that a high vapor content condition at the inlet can exert a substantial influence on the heat transfer mechanism in both nucleate boiling and convective boiling regions. Supporting this assertion, Ganesan et al. [27] discovered and reported the diminished HTC dependence on Bo at high vapor content due to the appreciable boiling suppression. A similar data trend highlighting the impact of vapor content at the inlet is also discernible within the consolidated saturated HTC database. Fig. 7(a) depicts the variation in measured saturated HTC, $h_{tp,meas}$, with respect to the saturation length ratio for all local saturated HTC datapoints from the saturated HTC database. It is notable that a discernible trend is not apparent until the saturation length ratio reaches $\Delta z_{sat}/L_H = 1$. However, as the saturation length ratio surpasses unity ($\Delta z_{sat}/L_H > 1$), a distinct downward slope becomes evident. This downward slope serves as a clear indicator of the diminishing local saturated HTC with an increase in the saturation length ratio. From a qualitative standpoint, it is clear that the nucleate boiling HTC, h_{NB}, experiences significant suppression in

Table 2
Summary of the consolidated LN_2 database including experimental and historical HTC datasets.

	No. of datapoints in each subset of the database				
	Terrestrial Saturated HTC	Terrestrial Subcooled HTC	Terrestrial Single-phase liquid HTC	Microgravity Saturated HTC	Microgravity Subcooled HTC
Experimental dataset	2080	1436	636	86	102
Historical dataset	1751	104	5	0	0
Total	3831	1540	641	86	102

environments characterized by high vapor content. Contrary to the anticipated outcome of enhanced convective boiling leading to an increase in overall HTC, it is observed that the overall HTC diminishes with the increase in the saturation length ratio. This observation underscores a noteworthy flow boiling characteristic seemingly unique to cryogens, wherein nucleate boiling emerges as the dominant heat transfer mechanism, irrespective of the inlet conditions. Nonetheless, it is imperative to segregate datapoints associated with high vapor content conditions ($\Delta z_{sat}/L_H > 1$) from the database. Derived from an initial set of 3831 saturated HTC datapoints for LN_2, as indicated in Table 2, the segregation process has effectively yielded a refined subset comprising 3149 datapoints. This subset will be subjected to further analysis in subsequent stages of the study. As indicated in Fig. 7(a), 3,149 saturated

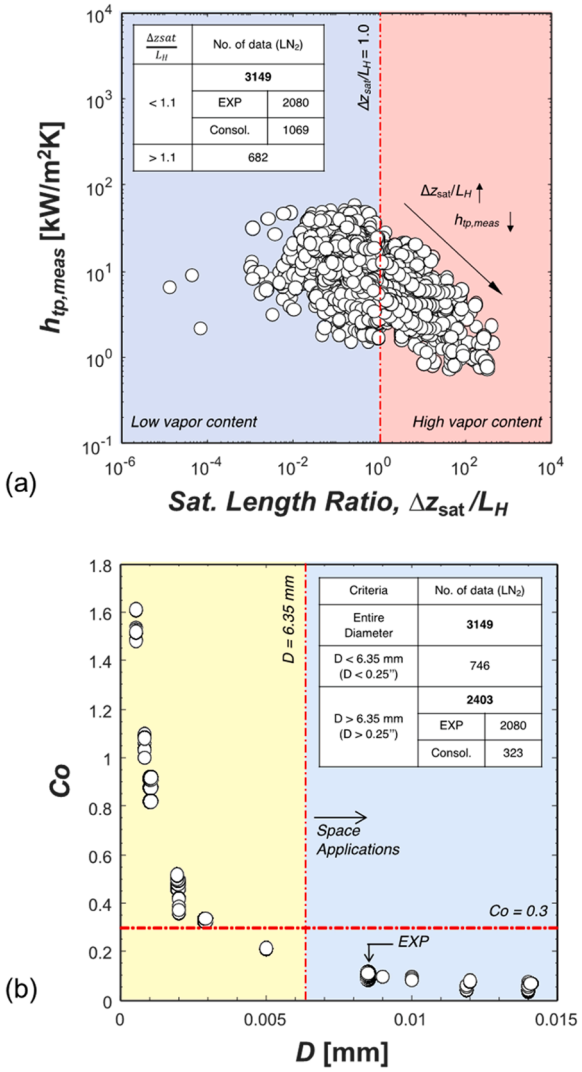

Fig. 7. Data demarcation based on (a) saturated length ratio, $\Delta z_{sat}/L_H$, and (b) tube diameter, D.

HTC datapoints have been categorized as low vapor content saturated HTC. Note that the new saturated HTC correlation, developed in a later section, will undergo rigorous testing not only for low vapor content conditions but will also be extended and tested comprehensively for high vapor content conditions. This comprehensive evaluation will substantiate the robustness and applicability of the correlation across a wide range of operating scenarios, thereby enhancing its utility and reliability.

Another simple yet very important physical segregation criterion is tube diameter, D. The two-phase flow pattern observed within a channel or a tube is inherently contingent upon the distribution of the different phases, which dynamically varies depending on specific geometry of the tubes. Due to the fundamental disparities in macroscale and microscale phase distributions [56], it is imperative to recognize that the associated heat transfer mechanisms also differ significantly. These discrepancies arise from the distinctive criteria governing the relative importance of various hydrodynamic forces, including inertia, viscosity, buoyancy, and surface tension effects, all of which exert considerable influence on the motion of liquid and vapor phases. In macroscale flows ($Co < 0.3$), gravity plays a pivotal role, whereas in microscale flows ($Co > 0.3$), the dominance of surface tension becomes increasingly pronounced, diminishing the influence of gravity. Confinement number, Co, which is defined as a ratio between the bubble length scale, $L_b(\sqrt{\sigma/((\rho_f - \rho_g)g)})$, and the channel diameter, D, is a commonly used parameter to assess the extent of bubble confinement within a given system. In perspective of the above, Ong and Thome [57] proposed confinement number criterion of $Co = 0.3$ as a threshold for distinguishing macro-channel and micro-channel flows. In Fig. 7(b), variation of confinement number, Co, with respect to tube diameter, D, is visually illustrated. As depicted, the transition from macroscale to microscale does not occur abruptly but instead gradually. Notice the increasing slope of the curve in Fig. 7(b) as Co exceeds 0.3, indicating significant change in dominancy among the hydrodynamic forces. Moreover, for all cryogenic space applications of interest, the plumbing dimensions typically exceed 6.35 mm (0.25 in), posing primary emphasis on macro-channel configurations. Considering the two pertinent facts: (1) the pronounced impact of gravity on heat transfer mechanisms in macro-channel flows with a confinement number, Co, less than 0.3, and (2) the prevalent use of large-sized plumbing with diameters exceeding 6.35 mm in cryogenic space applications, a further segregation of the saturated HTC database is undertaken. As exhibited in Fig. 7(b), out of the 3149 saturated HTC datapoints identified from Fig. 7(a), 2,403 datapoints having large tube diameter, $D >$ 6.35 mm, were extracted as a final database for the development of the new correlation. Recall that the primary objective of the present study is to construct robust and reliable flow boiling HTC correlations particularly suited for future cryogenic space applications.

Fig. 8 shows the local HTC data, normalized as $h_{tp,meas}/h_{sp,f}$ (ratio of measured saturated HTC to single-phase liquid HTC), versus the phase separation parameter $1/X_{tt}$, where X_{tt} is defined as

$$X_{tt} = \left(\frac{1-x_e}{x_e}\right)^{0.9}\left(\frac{\rho_g}{\rho_f}\right)^{0.5}\left(\frac{\mu_f}{\mu_g}\right)^{0.1} \tag{11}$$

The phase separation parameter, $1/X_{tt}$, was postulated by Ganesan et al. [27] and subsequently tested by Kim et al. [45] to explicitly

validate the presence of a convective boiling mechanism in cryogenic flow boiling. In this study, the same approach is adopted and applied to assess the saturated HTC database, with the results visually depicted in Fig. 8. Notably, when $1/X_{tt}$ is less than 0.1, the curve exhibits no reliance on the phase separation parameter, $1/X_{tt}$, indicating the two-phase heat transfer is dominated by nucleate boiling rather than convective boiling. The dominancy of nucleate boiling in this region can be attributed to the unique thermal properties of cryogenic fluids, namely low surface tension and latent heat of vaporization, which aid in sustaining bubble nucleation under low wall superheat. However, as $1/X_{tt}$ increases, which implies increased phase separation, the slope of the curve begins to increase, from near zero for $1/X_{tt} < 0.1$ to a non-zero positive value for the intermediate range of $0.1 < 1/X_{tt} < 1$. Furthermore, as $1/X_{tt}$ exceeds unity, a significant increase in slope becomes evident, indicating an enhanced contribution of convective boiling to the overall HTC. Therefore, by witnessing the relation between $h_{tp,meas}/h_{sp,f}$ and the phase separation parameter, it becomes logical to conceive that the functional form for the enhancement factor, F, commonly used in HTC correlation, is $F \sim f(1/X_{tt})$. This relationship will be revisited and incorporated in the new saturated HTC correlation in a subsequent section.

3.2. Assessment of prior saturated HTC correlations

3.2.1. Assessment of seminal correlations

A list of seminal saturated flow boiling HTC correlations is compiled in Table 3, along with notable remarks regarding flow orientation, working fluids and the functional form of h_{NB}. Notice how h_{NB} functional form can be broadly categorized into two main groups: (i) h_{NB} depending on pool boiling HTC, h_{PB}, supplemented with the *suppression factor, S*, which is a function of G and x_e, and (ii) h_{NB} represented by a single-phase liquid HTC, $h_{sp,f}$, supported with combination of Bo, Pr_f, and $(1\text{-}x_e)$. Note that these two distinct functional forms are essentially equivalent but have been mathematically rearranged to better align with their respective interpretations of nucleate boiling physics. Specifically, the saturated HTC correlations developed by Chen [39], Liu and Winterton [36], and Steiner and Taborek [41] fall under the first category of the h_{NB} functional form, $f(h_{PB}, S)$. These correlations utilize pool boiling correlations proposed by Foster and Zuber [58], Cooper [59], and Gorenflo and Sokol [60], respectively. Conversely, the second functional form, $f(h_{sp,f}, Bo, Pr_f, (1\text{-}x_e))$, was employed by Shah [43], Gungor and Winterton [35], Kim and Mudawar [44], and Ganesan et al. [27]. Note that the HTC correlation developed by Kim and Mudawar was based on micro-channel HTC database which does not align with the present HTC database for large diameters. In addition to the mentioned correlations, another saturated HTC correlation, proposed by Fang et al. [61], has been taken into account as a separate and distinct third group. Interestingly, this correlation deviates from employing a superposition-type functional form, distinguishing itself within the spectrum of considered correlations. The functional form of the correlation by Fang et al. [61] can be found in Table 3.

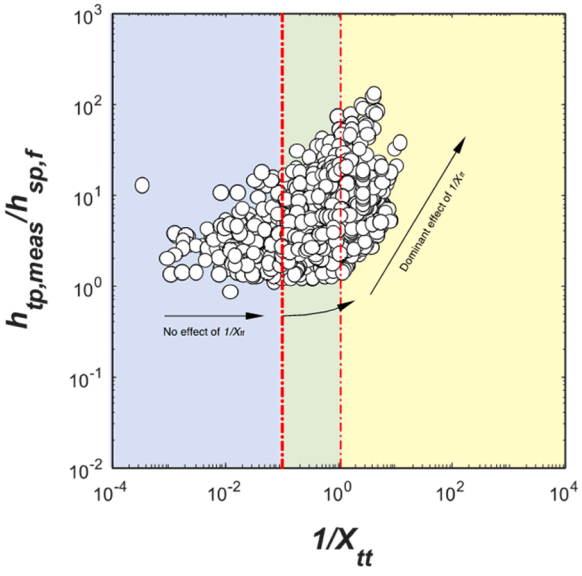

Fig. 8. Variation of ratio of measured two-phase HTC to single-phase liquid HTC with phase separation parameter, $1/X_{tt}$.

The performance of the seminal flow boiling HTC correlations is tested and compared to the demarcated saturated HTC database. The predictive accuracy of each correlation is assessed by evaluating mean absolute error (MAE) which is defined for local HTC as

$$MAE = \frac{1}{N}\sum \frac{\left|h_{tp,pred} - h_{tp,meas}\right|}{h_{tp,meas}} \times 100\ [\%] \tag{12}$$

The overall MAE of each correlation will be used to determine the most accurate correlation for the database.

3.2.2. Assessment results and discussion

Fig. 9 presents parity plots for the comprehensive evaluation of seminal saturated flow boiling correlations. Among these, two correlations emerge as the top performers, exhibiting MAE values of 28.88 % and 28.89 %, for Liu and Winterton [36] and Ganesan et al. [27], respectively. Liu and Winterton's correlation is constructed upon the functional form $f(h_{PB}, S)$, which incorporates Cooper's pool boiling correlation [59] as its foundation, effectively compensated by the suppression factor, S. This compensatory mechanism aims to address the diminishing influence of nucleate boiling with increasing G and x_e. While the majority of datapoints exhibit predictions that closely align with the 45° diagonal line, signifying reasonably accurate predictions, there are isolated datapoints in the top-left region that deviate beyond the +50 % boundary. The overprediction of these specific datapoints not only indicates an inadequate suppression of the nucleate boiling HTC but also an inaccurate prediction stemming from Cooper's pool boiling correlation, which significantly overestimates these specific datapoints. Nevertheless, Liu and Winterton's correlation demonstrates its capability in predicting the current cryogenic saturated HTC database with a reasonable degree of accuracy. In contrast, Ganesan et al.'s correlation [27] is formulated based on the functional expression $f(h_{sp,f}, Bo, Pr_f, (1\text{-}x_e), Co)$. A noteworthy feature of this correlation is the commendable alignment of datapoints observed along the 45° diagonal line. This alignment results in a substantial portion of the local HTC data falling within the ±50 % boundaries. However, as elucidated by Kim et al. [47], concerns have been raised regarding the applicability of this correlation in microgravity conditions due to the inclusion of the Confinement number, Co, which is inversely proportional to the square root of gravity, rendering it unsuitable for microgravity scenarios. Nevertheless, under $1\text{-}g_e$ condition, Ganesan et al.'s correlation [27] maintains its proficiency in predicting cryogenic saturated HTC data with an acceptable degree of accuracy. Subsequently, following the two most accurate correlations, those by Chen [39], Klimenko [40], Steiner Taborek [41], and Kim and Mudawar [44] exhibit MAE values within the range of 30 to 40 %. Notably, Chen's correlation, despite displaying a relatively lower level of accuracy compared to the top-performing models, shows favorable clustering of data. This earliest of the seminal correlation considered, relies on the pool boiling HTC correlation developed by Foster and Zuber [58], which, as documented by Kim et al. [45,47], provides significantly improved predictions compared to Cooper's pool boiling correlation [59] for both terrestrial and microgravity saturated HTC data. Within the framework of Chen's correlation, there appears to be untapped potential for further refinement, particularly with respect to the functional form of the suppression factor. Another correlation of the $f(h_{PB}, S)$ type, proposed by Steiner and Taborek [41], also exhibits favorable data clustering with a reasonable alignment

Table 3
Prior seminal saturated HTC correlations.

Author(s)	Correlation	Remarks
Chen [39]	$h_{tp} = h_{NB} + h_{CB}$ $\frac{h_{NB}}{h_{PB}} = S$ $\frac{h_{CB}}{h_{sp,f}} = F$ where $h_{sp,f} = 0.023 Re_{f,D}^{0.8} Pr_f^{0.4} \frac{k_f}{D}$ $h_{PB} = 0.0015 Re_b^{0.62} Pr_f^{0.33} \frac{k_f}{R_b}$ $Re_b = \frac{\pi}{Pr_f}\left(\frac{\rho_f}{\rho_g} Ja\right)^2$ $R_b = \frac{\Delta T_{sat}}{h_{fg}\rho_g}\sqrt{\frac{2\pi k_f \rho_f c_{p,f}\sigma}{\Delta P_{sat}}}\sqrt[4]{\frac{\rho_f}{\Delta P_{sat}}}$ For $1/X_{tt} \le 0.1$, $F = 1$ For $1/X_{tt} > 0.1$, $F = 2.35\left(0.213 + \frac{1}{X_{tt}}\right)^{0.736}$ $S = \frac{1}{1 + 2.53\times10^{-6}(Re_{f,D}F^{1.25})^{1.17}}$	• Flow orientation: vertical upflow and downflow • Fluids: water, methanol, cyclohexane, pentane, heptane, benzene • Functional form for hNB : f(hPB, S)
Shah [43]	$\frac{h_{tp}}{h_{sp,f}} = \max\left\{\frac{h_{NB}}{h_{sp,f}}, \frac{h_{CB}}{h_{sp,f}}\right\}$ where $h_{sp,f} = 0.023 Re_{f,D}^{0.8} Pr_f^{0.4} \frac{k_f}{D}$ $\frac{h_{CB}}{h_{sp,f}} = F = 1.8/N^{0.8}$ For vertical flow, $N = N_{conv.}$ For horizontal flow, if $Fr_{fo,D} \ge 0.04$, $N = N_{conv.}$ if $Fr_{fo,D} < 0.04$, $N = 0.38(Fr_{fo,D})^{-0.3} N_{conv.}$ For $N > 1$ if $Bo > 3\times10^{-5}$, $\frac{h_{NB}}{h_{sp,f}} = 230 Bo^{0.5}$ if $Bo < 3\times10^{-5}$, $\frac{h_{NB}}{h_{sp,f}} = 1 + 46 Bo^{0.5}$ For $0.1 < N \le 1$ $\frac{h_{NB}}{h_{sp,f}} = FBo^{0.5}\exp(2.74N^{-0.1})$ For $N \le 0.1$ $\frac{h_{NB}}{h_{sp,f}} = FBo^{0.5}\exp(2.47N^{-0.15})$ where $F = 14.7$, if $Bo \ge 11\times10^{-4}$ $F = 15.43$, if $Bo < 11\times10^{-4}$	• Flow orientation: vertical upflow, vertical downflow, horizontal flow • Fluids: water, R11, R12, R22, R113, R505, cyclohexane, ammonia, n-butyl alcohol, isopropyl alcohol, aqueous solutions of potassium carbonate • Functional form for h_{NB} : $f(h_{sp,f}, Bo)$
Gungor and Winterton [35]	$\frac{h_{tp}}{h_{sp,f}} = E + \frac{h_{NB}}{h_{sp,f}} + \frac{h_{CB}}{h_{sp,f}}$ $\frac{h_{NB}}{h_{sp,f}} = 3000 EBo^{0.86}$ $\frac{h_{CB}}{h_{sp,f}} = F = 1.12E\left(\frac{x_e}{1-x_e}\right)^{0.75}\left(\frac{\rho_f}{\rho_g}\right)^{0.41}$ where $h_{sp,f} = 0.023 Re_{f,D}^{0.8} Pr_f^{0.4} \frac{k_f}{D}$ For vertical flow, $E = 1$ For horizontal flow, if $Fr_{fo,D} \ge 0.05$, $E = 1$ if $Fr_{fo,D} < 0.05$, $E = Fr_{fo,D}^{(}0.1 - 2Fr_{fo,D})$	• Flow orientation: vertical upflow, vertical downflow, horizontal flow • Fluids: Water, R11, R12, R113, R114, R22, ethylene glycol • Functional form for hNB : f(hsp,f, *Bo*)
Klimenko [40]	$h_{tp} = \max\{h_{NB}, h_{CB}\}$ $h_{NB} = C\left(\frac{qLa_D}{h_{fg}\rho_g\alpha_f}\right)^{0.6}\left(\frac{PLa_D}{\sigma}\right)^{0.54} Pr_f^{-0.33}\left(\frac{k_w}{k_f}\right)^{0.12}\frac{k_f}{La_D}$ $h_{CB} =$ $0.087\left(\frac{G}{\rho_f}\left[1 + x_e\left(\frac{\rho_f}{\rho_g} - 1\right)\right]\frac{La_D}{\nu_f}\right)^{0.6} Pr_f^{1/6}\left(\frac{\rho_g}{\rho_f}\right)^{0.2}\left(\frac{k_w}{k_f}\right)^{0.09}\frac{k_f}{La_D}$ where $C = 6.1\times10^{-3}$ for cryogenic fluids $La_D = \sqrt{\frac{\sigma}{g(\rho_f - \rho_g)}}$	• Flow orientation: vertical upflow, vertical downflow, horizontal flow • Fluids: water, R11, R12, R113, R114, R22, NH3, propane, butane, pentane, peptane, isooctane, benzene, cyclohexane, methanol, ethanol, LHe, LH2, LNe, LN2, LAr • Functional form for h_{NB} : $f(h_{PB})$, assuming no boiling suppression, $S = 1$
Liu and Winterton [36]	$h_{tp}^2 = h_{NB}^2 + h_{CB}^2$ $\frac{h_{NB}}{h_{PB}} = S = E_{NB}\left[1 + 0.055\left(1 + x_e Pr_f\left(\frac{\rho_f}{\rho_g} - 1\right)\right)^{0.035} Re_{fo,D}^{0.16}\right]^{-1}$	• Flow orientation: vertical upflow, vertical downflow, horizontal flow • Fluids: water, R11, R12, R113, R114, R22, ethylene glycol, n-butanol, ethanol • Functional form for hNB : f(hPB, S)

(*continued on next page*)

Table 3 (*continued*)

Author(s)	Correlation	Remarks
	$\frac{h_{CB}}{h_{sp,fo}} = F = E_{CB}\left[1 + x_e Pr_f\left(\frac{\rho_f}{\rho_g} - 1\right)\right]^{0.35}$ where $h_{sp,fo} = 0.023 Re_{fo,D}^{0.8} Pr_f^{0.4} \frac{k_f}{D}$ $h_{PB} = 55 P_R^{0.12} (-\log_{10} P_R)^{-0.55} q^{2/3} M^{-0.5}$ For vertical flow, $E_{NB} = E_{CB} = 1$ For horizontal flow, if $Fr_{fo,D} \geq 0.05$, $E_{NB} = E_{CB} = 1$ if $Fr_{fo,D} < 0.05$, $E_{CB} = Fr_{fo,D}^{(} 0.1 - 2Fr_{fo,D})$ $E_{NB} = Fr_{fo,D}^{0.5}$	
Steiner and Taborek [41]	$h_{tp}^3 = h_{NB}^3 + h_{CB}^3$ $\frac{h_{NB}}{h_{NB,o}} = F_P [q/q_o]^n [D/D_o]^{-0.4} [R_p/R_{p,o}]^{0.133} F_M$ $\frac{h_{CB}}{h_{sp,fo}} = F = \left[(1 - x_e)^{1.5} + 1.9 x_e^{0.6} \left(\frac{\rho_f}{\rho_g}\right)^{0.35}\right]^{1.1}$ where $h_{sp,fo} = \frac{(f_{sp,f}/8)(Re_{fo,D} - 1000) Pr_f}{1 + 12.7 (f_{sp,f}/8)^{0.5} (Pr_f^{2/3} - 1)} \frac{k_f}{D}$ $f_{sp,f} = [0.7904 \ln Re_{fo,D} - 1.64]^{-2}$ Standard reference conditions: $P_{R,o} = 0.1$, $R_{p,o} = 1$ μm, $D_o = 0.01$ m, and, For LHe, $q_o = 1000$ W/m^2, $h_{NB,o} = 1990$ W/m^2-K, $F_M = 0.86$ For LH_2, $q_o = 10{,}000$ W/m^2, $h_{NB,o} = 12{,}220$ W/m^2-K, $F_M = 0.35$ For LNe, $q_o = 10{,}000$ W/m^2, $h_{NB,o} = 8920$ W/m^2-K, $F_M = 0.98$ For LN_2, $q_o = 10{,}000$ W/m^2, $h_{NB,o} = 4380$ W/m^2-K, $F_M = 0.8$ For LAr, $q_o = 10{,}000$ W/m^2, $h_{NB,o} = 3870$ W/m^2-K, $F_M = 1.15$ For LCH_4, $q_o = 20{,}000$ W/m^2, $h_{NB,o} = 8060$ W/m^2-K, $F_M = 0.93$ For $P_R < 0.95$, $F_P = 2.816 P_R^{0.45} + (3.4 + 1.7/(1 - P_R^7)) P_R^{3.7}$ For LH_2, LNe, LN_2, LAr, $n = 0.7 - 0.13\exp(1.105 P_R)$ For LHe and LCH_4, $n = 0.8 - 0.1\exp(1.75 P_R)$	• Flow orientation: vertical upflow • Fluids: R11, R12, R113, R22, benzene, n-pentane, n-heptane, cyclohexane, methanol, n-butanol, ammonia, LHe, LH2, LN2 • Functional form for h_{NB} : $f(h_{PB})$, assuming no boiling suppression, $S = 1$
Kim and Mudawar [44]	$h_{tp}^2 = h_{NB}^2 + h_{CB}^2$ $\frac{h_{NB}}{h_{sp,f}} = \left[2345 \left(Bo \frac{P_H}{P_F}\right)^{0.7} P_R^{0.38} (1 - x_e)^{-0.51}\right]$ $\frac{h_{CB}}{h_{sp,f}} = F = \left[5.2 \left(Bo \frac{P_H}{P_F}\right)^{0.08} We_{fo,D}^{-0.54} + 3.5 \left(\frac{1}{X_{tt}}\right)^{0.94} \left(\frac{\rho_g}{\rho_f}\right)^{0.25}\right]$ where $h_{sp,f} = 0.023 Re_{f,D}^{0.8} Pr_f^{0.4} \frac{k_f}{D}$ For uniformly heated round tube, $pH = P_F = D$	• Flow orientation: vertical upflow, vertical downflow, horizontal flow • Fluids: water, FC72, R11, R113, R123, R1234yf, R1234ze, R134a, R152a, R22, R236fa, R245fa, R32, R404A, R407C, R410A, R417A, CO2 • Functional form for hNB : f(hsp,f, Bo, PR, (1-xe)) • Based on microchannel database
Ganesan et al. [27]	$h_{tp}^2 = h_{NB}^2 + h_{CB}^2$ if $\Delta Z_{sat}/L_H \leq 1.1$ $\frac{h_{NB}}{h_{sp,f}} = [1226 (Bo)^{0.81} P_R^{-0.05} (1 - x_e)^{-0.67} Co^{-0.06}]$ $\frac{h_{CB}}{h_{sp,f}} = \left[0.55 \left(\frac{1}{X_{tt}}\right)^{0.39} \left(\frac{\rho_g}{\rho_f}\right)^{-0.37} Co^{-1.39}\right]$ if $\Delta Z_{sat}/L_H > 1.1$ $\frac{h_{NB}}{h_{sp,f}} = [562 (Bo)^{0.57} P_R^{0.02} (1 - x_e)^{-0.76}]$ $\frac{h_{CB}}{h_{sp,f}} = \left[0.51 \left(\frac{1}{X_{tt}}\right)^{0.41} \left(\frac{\rho_g}{\rho_f}\right)^{0.42}\right]$ $h_{sp,f} = \frac{(4f_{sp,f}/8)(Re_{f,D} - 1000) Pr_f}{1 + 12.7 (4f_{sp,f}/8)^{0.5} (Pr_f^{2/3} - 1)} \frac{k_f}{D}$ $4f_{sp,f} = [0.7904 ln Re_{f,D} - 1.64]^{-2}$	• Flow orientation: vertical upflow, vertical downflow, horizontal flow • Fluids: LHe, LH2, LNe, LN2, LAr, LCH4 • Functional form for hNB : • hNB = f(hsp,f, Bo, PR, (1-xe), Co) for Δzsat/LH ≤ 1.1 • hNB = f(hsp,f, Bo, PR, (1-xe)) for Δzsat/LH > 1.1 • Based on terrestrial cryogenic data only
Fang et al. [61]	$h_{tp} = \left(\frac{k_f}{D}\right) F_f M^{-0.18} Bo^{0.98} Fr_{fo}^{0.48} Bd^{0.72} \left(\frac{\rho_f}{\rho_g}\right)^{0.29} \left[\ln\left(\frac{\mu_f}{\mu_w}\right)\right]^{-1} Y$ $Y = \begin{cases} 1 & for\ P_r \leq 0.43 \\ 1.38 - P_r^{1.15} & for\ P_r > 0.43 \end{cases}$ $F_f = 1715$ for LN_2	• Flow orientation: vertical upflow, horizontal flow, inclined flow • Fluids: R134a, R1234yf, R22, R410A, R32, R407C, R404A, R507, R1234ze(E), R417A, LN2, R290, R123, R717, R245fa, R600a, R152a, CO2 • Non-superposition type correlation • μ_w evaluated at inner wall temperature (Tw) • μ_f evaluated at fluid temperature (Tf)

toward the 45° diagonal line. This correlation employs the pool boiling correlation by Gorenflo and Sokol [60]. However, it is important to note that Steiner and Taborek's correlation, unlike others evaluated, is not universal due to its reliance on distinct empirical constants for different cryogenic fluids. Similarly, Klimenko's correlation [40], despite delivering accurate predictions for terrestrial data, falters under microgravity conditions due to the numerical divergence of the Laplace length ratio, *La*, as gravity approaches zero. Moving on to the least performing correlations, those by Shah [43] and Gungor and Winterton [35] exhibit MAE values of 40.48 % and 52.44 %, respectively. These correlations are notably deficient in accurately representing the suppression of nucleate boiling phenomena, resulting in a propensity to overestimate the HTC under high heat flux conditions. Lastly, as documented in Table 4, the correlation developed by Fang et al. [61] demonstrates commendable

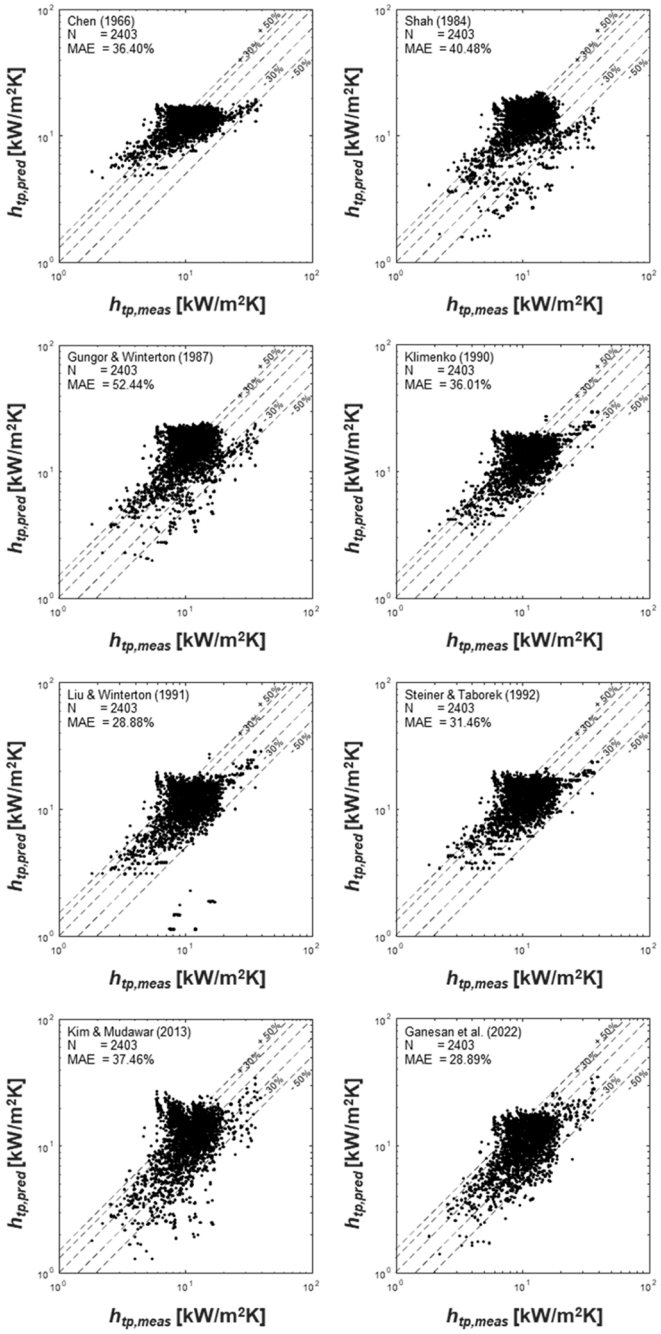

Fig. 9. Performance of seminal saturated flow boiling HTC correlations against demarcated saturated HTC data for LN_2 under terrestrial gravity.

predictive capabilities when assessed against the 1 g terrestrial LN_2 database of the current study, yielding an MAE of 24.75 %. This accuracy stands out as the highest among the selected seminal correlations. The correlation leverages the dimensionless group (μ_f/μ_w), which provides the capability to trace HTC variations across diverse fluid types. Despite the outstanding performance of the correlation, Fang et al.'s correlation [61] is subject to certain limitations attributed to the following considerations. First, in microgravity conditions, as g→0, the correlation significantly underestimates LN_2 HTC, registering an MAE of 96.11 %, owing to the inclusion of gravitational acceleration terms in Fr_{fo} and Bd. Second, although demonstrating favorable performance for LN_2 and LAr, the correlation struggles to accurately predict heat transfer coefficients for LHe, suggesting a lack of universal applicability, at least, to cryogenic fluids. Third, the correlation adopts an implicit functional form based on the dimensionless group (μ_f/μ_w), requiring wall temperature information to retrieve dynamic viscosity at the local wall temperature. The inherent implicit nature of the correlation may pose challenges in its integration into design codes. Nevertheless, under 1-g_e condition, Fang et al.'s correlation [61] demonstrates notable proficiency in accurately predicting cryogenic saturated HTC data.

Evaluation statistics are comprehensively summarized in Table 4, which not only covers the finalized saturated HTC database but also includes extended databases for LN_2 with fewer segregation criteria applied.

3.3. New saturated HTC correlation

3.3.1. Development rationale

The assessment conducted in Section 3.2.2, coupled with the statistics presented in Table 4, provides a noteworthy observation regarding the performance of the correlation proposed by Ganesan et al. [27]. While this correlation demonstrates commendable predictive accuracy when applied to the final demarcated database, it exhibits a notable deficiency in accurately predicting the microgravity data. Consequently, there exist no robust saturated HTC correlation for cryogenic flow boiling which can provide reliable predictions for a wide range of gravity levels, albeit its high importance and demand for space applications, as emphasized in the Introduction. Therefore, the aforementioned observations provide a compelling rationale for the imperative need to develop an updated and enhanced saturated HTC correlation possessing the intrinsic capability to deliver accurate predictions across a broad spectrum of gravity levels, effectively addressing the pivotal requirements of space-related applications.

3.3.2. Formulation of correlation for saturated flow boiling HTC

According to prior experimental results acquired by the present authors [46], it was reported that heat transfer coefficient curves commonly exhibit a sharp and almost linearly increasing trend with increasing heat flux in the lower heat flux range. Subsequently, the slope of the curves progressively decreases, displaying comparatively moderate changes in HTC until CHF. The strong correlation between the HTCs and the wall heat flux suggests that the dominant heat transfer mechanism in this regime is nucleate boiling. The gradually decreasing slope of the HTC curve is a result of the suppression of nucleate boiling. The observed experimental trend and the analysis of functional forms employed in previous correlations highlights the advantages of utilizing a superposition-type correlation that incorporates the nucleate boiling HTC formulated with pool boiling HTC, h_{PB}, and suppression factor, S, by which a favorable data cluster was achieved against the demarcated saturated HTC database. Note that the enhancement factor, F, is employed and multiplied to the single-phase liquid heat transfer coefficient, $h_{sp,f}$. The enhancement factor addresses the growing influence of convective heat transfer on the two-phase heat transfer coefficient as phase separation increases, as discussed in Section 3.1 and depicted in Fig. 8. Therefore, the functional form for saturated HTC, h_{tp}, is selected as

$$h_{tp}^{\ 2} = [f(h_{PB}, S)]^2 + [f(h_{sp,f}, F)]^2 \tag{13}$$

3.3.2.1. Suppression factor, S. In order to examine the effect of the nucleate boiling suppression, the suppression factor, S, is evaluated as

$$S = \left(\frac{h_{tp,meas} - h_{CB,Ganesan}}{h_{PB}}\right) \tag{14}$$

where $h_{tp,meas}$ is measured local saturated HTC, h_{CB} is convective boiling HTC calculated based on Ganesan et al.'s correlation [27], and h_{PB} is based on Forster and Zuber's pool boiling correlation [58]. Fig. 10(a) provides insight into the behavior of the suppression factor, S, in relation

Table 4
Data demarcation and prediction statistics for seminal HTC correlations and the new correlation for saturated flow boiling regime.

Dataset		*N*	New Saturated correlation	Chen (1966)	Shah (1984)	Gungor & Winterton (1987)	Klimenko (1991)	Liu & Winterton (1991)	Steiner & Taborek (1992)	Kim & Mudawar (2013)	Fang et al. (2017)	Ganesan et al. (2022)
			MAE [%]	*MAE* [%]	*MAE* [%]	*MAE* [%]	*MAE* [%]	*MAE* [%]	*MAE* [%]	*MAE* [%]	*MAE* [%]	*MAE* [%]
LN_2 Database	Entire 1-g_e dataset	3831	27.61	52.13	50.98	61.47	37.04	32.79	46.61	39.87	24.63	27.50
	Dataset with • $\Delta z_{sat}/L_H < 1.1$	3149	26.79	54.53	52.07	65.68	37.39	32.10	50.44	36.97	20.97	26.82
	Dataset with • $\Delta z_{sat}/L_H < 1.1$ • $D > 6.35$ mm	2403	23.84	36.40	40.48	52.44	36.01	28.88	31.46	37.46	24.75	28.89
	Microgravity	86	16.73	17.07	21.91	28.19	110.54	24.20	20.02	25.52	96.11	52.59
LN_2 LHe LAr	Dataset with • $\Delta z_{sat}/L_H < 1.1$ • $D > 6.35$ mm	2445	24.01	37.78	40.01	52.82	38.16	31.14	33.43	38.15	26.33	29.87

to the dimensionless parameter Bo^2We. The formulation of Bo^2We serves to isolate the influence of q''. This parameter can also encapsulate the effect of x_e since x_e is directly proportional to q'', based on energy balance. Within Fig. 10(a), a discernible trend emerges, illustrating a gradual reduction in the suppression factor, S, ranging between 10^0 and 10^{-1}. The gradual decrease in S as Bo^2We increases signifies a diminishing impact of nucleate boiling under conditions characterized by high q'' or high x_e. These conditions correspond to scenarios where vapor content is high, leading to the suppression of bubble nucleation at the wall. It should be noted that when S equals unity, it signifies the absence of nucleate boiling suppression, whereas S values less than unity indicate effective suppression of nucleate boiling, resulting in lower h_{NB} compared to h_{PB}. To capture the observed trend of S as a function of Bo^2We, the Sigmoid function ($y = 1/[1 + e^x]$) has been employed. The resultant suppression factor function is visually depicted as the red line in Fig. 10(a). It can be clearly observed that the formulated suppression factor function, the red line, well tracks the suppression data trend. In contrast, in Fig. 10(b), the suppression factor for high pressure HTC data, marked by P_R values exceeding 0.41, shows a distinct trend from that observed in lower system pressure, Fig. 10(a). Under the high system pressure conditions, local h_{NB} is not effectively suppressed; instead, measured trend of S aligns well with $S = 1$, as indicated in Fig. 10(b). Therefore, an alternative function for S has to be introduced as $S = 1$ for high system pressure operating conditions, $P_R > 0.41$.

3.3.2.2. Gravitational parameter. As highlighted in Section 3.3.1, the primary objective of the new saturated HTC correlation is to encompass a broad range of gravitational acceleration conditions, with a particular emphasis on the extreme case of reduced gravity ($g \to 0$). According to prior experimental results acquired by the present authors [46,47], it was reported that HTC values in a microgravity environment tend to surpass those observed under terrestrial gravity. The enhancement of microgravity heat transfer coefficient in the low to intermediate heat flux range was attributed to the absence of buoyancy in the reduced gravity condition, which leads to earlier bubble nucleation and faster bubble growth compared to terrestrial gravity conditions. Moreover, under microgravity, the generated void fraction was observed to be much larger than in the same operating conditions under Earth gravity, resulting in improved heat transfer due to faster flow and intensified turbulence. However, in the high heat flux range, the microgravity HTC became comparable to that obtained in 1-g_e vertical upflow orientation, while remaining higher than the HTC values observed in other orientations, including horizontal, 45° inclined upflow, 45° inclined downflow, and vertical downflow. To effectively account for the HTC variations induced by gravity level, it is straightforward to introduce an additional parameter into the functional form of the h_{NB}. This necessitates the formulation of an appropriate functional form, which is proposed as

$$\left[tanh\left(\frac{g_e}{g}\right)\right]\left[1+\frac{1}{Fr_{fo}^{**}}\right]^n \tag{15}$$

$$Fr_{fo}^{**} = \frac{(G+800)^2}{\rho_f^2(g_e - g)D} \tag{16}$$

Notice the argument of the *tanh* function, represented as g_e/g, is the ratio of the terrestrial gravitational acceleration, g_e, to the gravitational acceleration of the specific system, g. As the gravity level decreases below Earth's gravity, the argument of the *tanh* function approaches infinity. Conversely, when the gravity level increases above Earth's gravity, the argument of the *tanh* function approaches zero. The behavior of the gravity ratio, g_e/g, sheds light on the trend exhibited by $tanh(g_e/g)$, which is depicted in Fig. 11. Under Earth's gravity, $tanh(g_e/g)$ is equal to $tanh(1)$, yielding a value of 0.76. As the gravity level approaches zero, $tanh(g_e/g)$ asymptotically approaches unity. This observation highlights the effectiveness of this parameter in capturing the HTC enhancement under microgravity conditions. However, it is important to exercise caution, particularly with regard to the decreasing behavior of this parameter under high gravity levels exceeding 9.81 m/s^2. This caution is based on the absence of hypergravity HTC data in the current database, which presents a challenge in verifying the decreasing $tanh(g_e/g)$ trend at high gravity levels. Consequently, the utilization of this parameter should be strictly confined to the range of $0 < g < 9.81$ m/s^2.

Furthermore, according to the reported experimental results [46,47], two additional trends were identified. First, there is a discernible decrease in HTC as mass velocity increases under microgravity conditions. Second, it was noted that the reduced gravity effect, which augments HTC, diminishes with the rise in mass velocity. In order to incorporate the observed mass velocity effect under microgravity into the gravity parameter, a modified liquid-only Froude number has been formulated, as exhibited in Eqs. (15) and (16). Through the integration

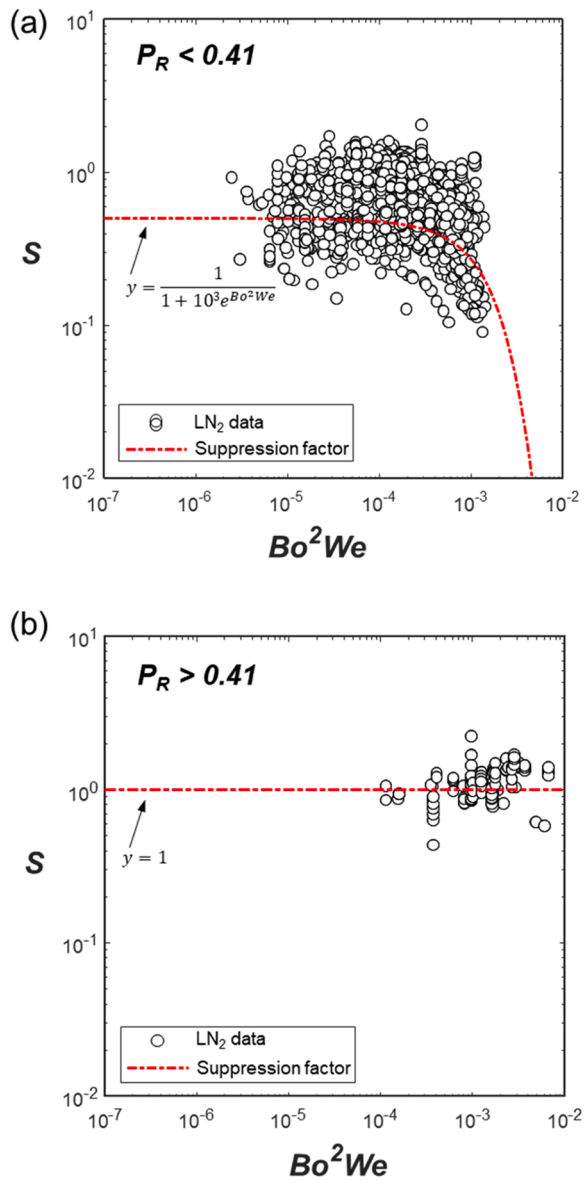

Fig. 10. Performance of proposed function to predict behavior of the suppression factor, S, with respect to dimensionless parameter Bo^2We for (a) lower pressure range, $P_R < 0.41$, and (b) higher pressure range, $P_R > 0.41$, for LN_2.

of the modified liquid-only Froude number with $tanh(g_e/g)$, the gravity parameter in Eq. (15) becomes capable of capturing the subdued impact of reduced gravity with increasing mass velocity. Note that the gravity component of the modified liquid-only Froude number, $(g_e\text{-}g)$, serves a dual purpose: (a) activating the mass velocity effect when gravitational acceleration, g, is less than Earth gravity, and (b) preventing numerical divergence as $g \rightarrow 0$. This ensures the stability and applicability of the gravity parameter across varying gravity fields. In conclusion, the functional form for h_{NB} can be expressed as

$$h_{NB} = f\left(h_{PB},\ tanh\left(\frac{g_e}{g}\right)\left[1+\frac{1}{Fr_{fo}^{**}}\right]^n,\ S\right) \tag{17}$$

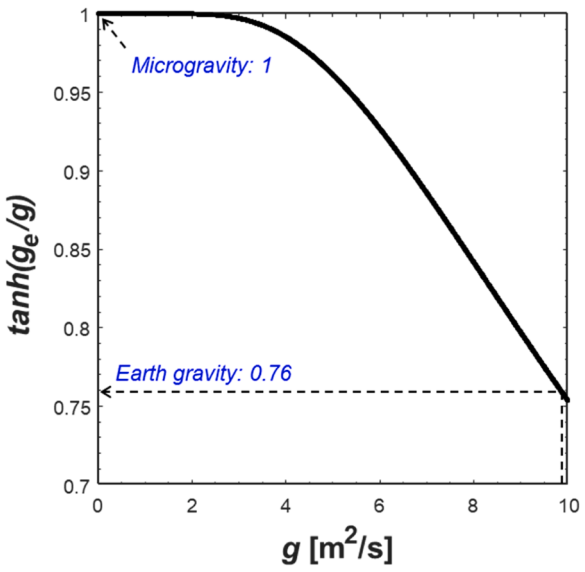

Fig. 11. Functional behavior of hyperbolic tangent function, $tanh\ (g_e/g)$, with respect to gravity, g.

3.3.2.3. Convective boiling heat transfer coefficient, h_{CB}. Lastly, the formulation of the functional form for h_{CB} is derived from both experimental data trends and previous correlations. As summarized by Ganesan et al. [27], it is observed that as void fraction, α, increases axially within the annular flow regime, the phase separation parameter, $1/X_{tt}$, also increases, driven by the rising x_e, and in tandem so does h_{CB}. This serial chain relation provides a theoretical foundation for the observed experimental trends, as depicted in Fig. 8. Based on this observation, the enhancement factor, $F(=h_{CB}/h_{sp})$, can be represented as $F \sim f(1/X_{tt})$, which suggests an escalating convective boiling contribution with increasing $1/X_{tt}$. Furthermore, based on prior correlations, as indicated in Table 3, the enhancement factor, F, is generally correlated with $1/X_{tt}$ [27,39,44], among other factors such as density ratio and reduced pressure. These additional factors are utilized to account for variations in fluid properties with pressure, across multiple fluids. Consequently, for the new correlation, h_{CB} is formulated according to the functional form

$$h_{CB} = f\left(h_{sp},\ F\left(\frac{1}{X_{tt}}\right),\ \left(\frac{\rho_f}{\rho_g}\right)\right) \tag{18}$$

Based on the analyzed results, the saturated heat transfer coefficient, h_{tp}, is expected to have the following functional form,

$$h_{tp}^2 = \left[h_{NB}^2 + h_{CB}^2\right]$$

$$h_{NB} = \begin{cases} C_1 \cdot h_{PB} \cdot \left[tanh\left(\frac{g_e}{g}\right)\right] \cdot \left[1+\frac{1}{Fr_{fo}^{**}}\right]^{C_2} \cdot \left[\frac{1}{1+C_3 \cdot \exp(Bo^2We)}\right]^{C_4} & P_R \le 0.41 \\ C_5 \cdot h_{PB} \cdot \left[tanh\left(\frac{g_e}{g}\right)\right] \cdot \left[1+\frac{1}{Fr_{fo}^{**}}\right]^{C_2} & P_R > 0.41 \end{cases}$$

$$h_{CB} = C_6 \cdot h_{sp,f} \cdot \left(\frac{1}{X_{tt}}\right)^{C_7} \cdot \left(\frac{\rho_f}{\rho_g}\right)^{C_8} \tag{19}$$

3.3.3. New correlation and its statistics

The final correlation is presented as

$$
\begin{aligned}
h_{tp}^{\ 2} &= \left[h_{NB}^{\ 2} + h_{CB}^{\ 2}\right] \\
h_{NB} &= \begin{cases} 1.36 \cdot h_{PB} \cdot \left[tanh\left(\frac{g_e}{g}\right)\right] \cdot \left[1 + \frac{1}{Fr_{fo}^{**}}\right]^{7.48} \cdot \left[\frac{1}{1 + 10^3 \cdot \exp(Bo^2 We)}\right]^{0.475} & P_R \le 0.41 \\ 1.20 \cdot h_{PB} \cdot \left[tanh\left(\frac{g_e}{g}\right)\right] \cdot \left[1 + \frac{1}{Fr_{fo}^{**}}\right]^{7.48} & P_R > 0.41 \end{cases} \\
h_{CB} &= 7 \cdot h_{sp,f} \cdot \left(\frac{1}{X_{tt}}\right)^{0.39} \cdot \left(\frac{\rho_f}{\rho_g}\right)^{-0.34} \\
h_{sp,f} &= \frac{\left(4f_{sp,f}/8\right)\left(Re_{f,D} - 1000\right)Pr_f}{1 + 12.7\left(\frac{4f_{sp,f}}{8}\right)^{0.5}\left(Pr_f^{2/3} - 1\right)} \frac{k_f}{D}
\end{aligned}
\tag{20}
$$

where the constants are regressed with an aim of minimizing the predictive error (the numerical regression is made certain to capture the global minima within the expected ranges), while preserving physical trends. The pool boiling HTC utilized by the new correlation, h_{PB}, is Forster and Zuber's [58]. The single-phase HTC utilized in the correlation, $h_{sp,f}$, is Gnielinski's [62]. The predictive performance of the newly developed correlation over the final demarcated LN_2 saturated HTC database is thoroughly presented, both statistically in Table 4 and visually in Fig. 12. In Fig. 12(a), the parity plot shows the alignment of the local HTC datapoints along the 45° diagonal lines and within ±50 % boundaries, resulting in an overall MAE of 23.84 % for the terrestrial gravity condition. Fig. 12(b) further highlights the exceptional predictive capability of this new correlation, showcasing an overall MAE of 16.73 % for microgravity conditions. The uniform performance of the new correlation over the extended databases with fewer or no segregation criteria (from the third row to the first row of Table 4), has to be pointed out. This superiority of the new correlation becomes even more apparent when compared to the summarized MAEs of the previous seminal correlations, where MAEs tend to significantly increase when applied to the extended datasets for LN_2 with fewer segregation criteria applied. Ganesan et al.'s correlation [27] is the only exception among the previous seminal correlations, showing relatively uniform accuracy over the databases, except for the microgravity database (the fourth row of Table 4), where it exhibits appreciable error. Thus, the superiority of the new correlation becomes more evident not only through its consistently low MAE across the databases but also its exceptional accuracy under microgravity conditions. In light of the comprehensive evaluation and analysis presented, it is clear that the newly developed correlation offers robust predictive accuracy across a wide spectrum of operating conditions, flow orientations, and across a broad range of gravity levels for liquid nitrogen.

3.3.4. Extension of the new correlation to other cryogens

In order to assess the universality of the correlation, an evaluation is conducted utilizing local saturated HTC datapoints obtained from diverse cryogenic fluids. Rigorous application of the same segregation criteria resulted in the demarcation of 2445 local saturated HTC datapoints, encompassing three distinct cryogens: liquid nitrogen (LN_2), liquid helium (LHe), and liquid argon (LAr). It should be noted that the availability of experimental cryogenic HTC data acquired from large-diameter tubes ($D > 6.35$ mm) is conspicuously limited. The considerable amount of historical saturated HTC data, extracted from the open literature, predominantly pertains to experiments conducted using smaller-diameter tubes ($D < 6.35$ mm), which are of limited value to space applications of cryogens. Nonetheless, as depicted in Fig. 13, the newly developed correlation exhibits an overall MAE of 24.01 %. This finding underscores the universal applicability of the newly established correlation, extending its effectiveness not only to LN_2 but also to other cryogenic fluids.

4. Subcooled heat transfer coefficient

4.1. Data demarcation

Given that all experimental cases begin with a subcooled liquid at the inlet of the test section, the 2072 experimental datapoints, segregated from Fig. 6 using the criteria $x_e = 0$, inherently possesses both single-phase liquid and subcooled boiling datapoints. Likewise, among 109 historical subcooled datapoints for LN_2 extracted from open literatures, there is a possibility of existence for single-phase liquid HTC data along with subcooled boiling HTC data. Consequently, it is essential to partition the dataset into boiling and non-boiling subsets. The initiation of bubble nucleation and the commencement of the subcooled boiling process occur when the local wall temperature, T_w, exceeds the required ONB (Onset of Nucleate Boiling) temperature, $T_{w,ONB}$. To facilitate this demarcation, Steiner and Taborek's ONB correlation [41], based on the Karlsruhe data bank [63] for all fluid classes, including LHe, LH_2, and LN_2, is employed and mathematically rearranged using the relation $q''_{ONB}/h_{sp,fo}$, resulting in the following relation for $T_{w,ONB}$,

$$q_{ONB} = \frac{2\sigma T_{sat} h_{sp,fo}}{R_{b,crit}\rho_g h_{fg}} \tag{21–1}$$

$$T_{w,ONB} = T_{sat} + \frac{2\sigma T_{sat}}{R_{b,crit}\rho_g h_{fg}} \tag{21–2}$$

where $R_{b,crit}$ is the critical bubble radius, which represents the maximum radius of a bubble ($=2\sigma/P_{sat}$) undergoing evaporation within the thermal boundary layer. Steiner and Taborek [41] recommended using $R_{b,crit} = 0.3$ μm for usual drawn tube materials. As visually depicted in Fig. 14, by applying the ONB criterion, a total of 1540 datapoints has been demarcated as a LN_2 subcooled dataset, leaving 641 datapoints as non-boiling, single-phase liquid HTC datapoints. The numbers of datapoints for each subset are summarized in Table 2. Furthermore, it is worth noting the scarcity of subcooled cryogen data within the body of cryogenic literature, especially when compared to the abundance of datapoints available for saturated cryogenic HTC, as indicated in Table 2. Nonetheless, the demarcated 1540 subcooled dataset will be utilized for following assessment of previous correlations and the development of a new subcooled HTC correlation.

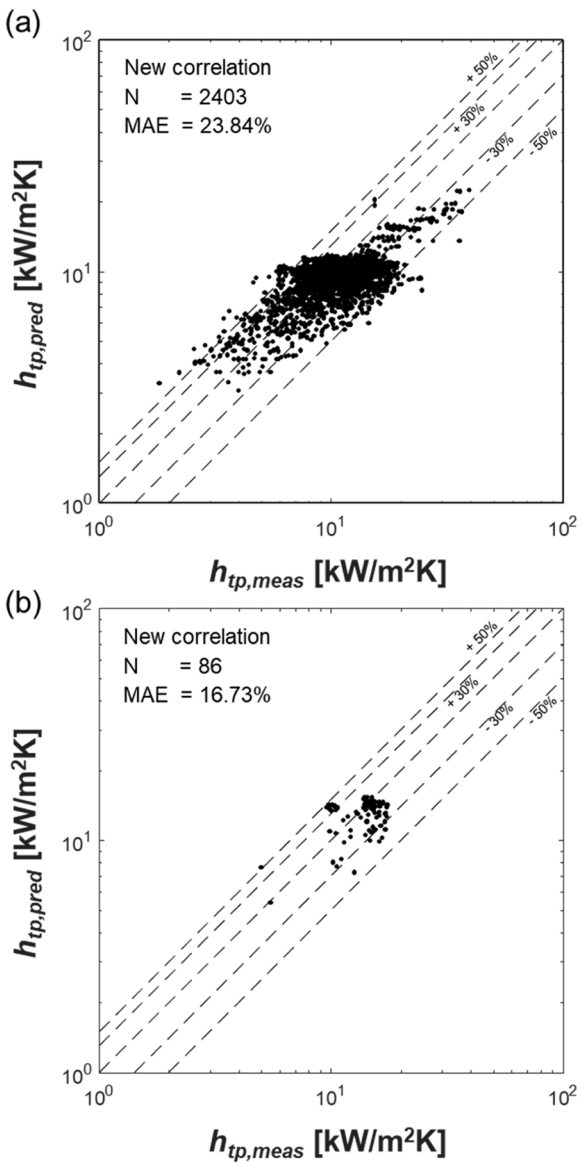

Fig. 12. Performance of the new saturated flow boiling HTC correlation against the demarcated (a) 1-g_e saturated HTC data, and (b) μg saturated HTC data for LN_2.

4.2. Assessment of prior subcooled HTC

4.2.1. Seminal subcooled HTC correlations

Representative seminal subcooled flow boiling HTC correlations are compiled in Table 5, along with notable remarks regarding flow orientation, working fluids, and utilized single-phase HTC correlations. Note that some equations are mathematically reformulated for consistency, but the recommendations of the original authors with respect to the choice of both single-phase and pool boiling correlations are adhered to. Notice how h_{sc} functional form can be broadly categorized into three different categories, (i) dimensionless-group-type correlation, like those of Papell [28], Moles and Shaw [31], and Devahdhanush and Mudawar [33], (ii) superposition type correlation, such as Liu and Winterton's [36], and (iii) intermediate type correlations like Shah's [38]. According to the recent study by Devahdhanush and Mudawar [33], it was determined that the dimensionless groups employed in Moles and Shaw's correlation produce the most accurate predictions for subcooled flow boiling across multiple fluids and applications. These applications included HFE-7100 in conventional-sized annuli [64], R-134a in parallel

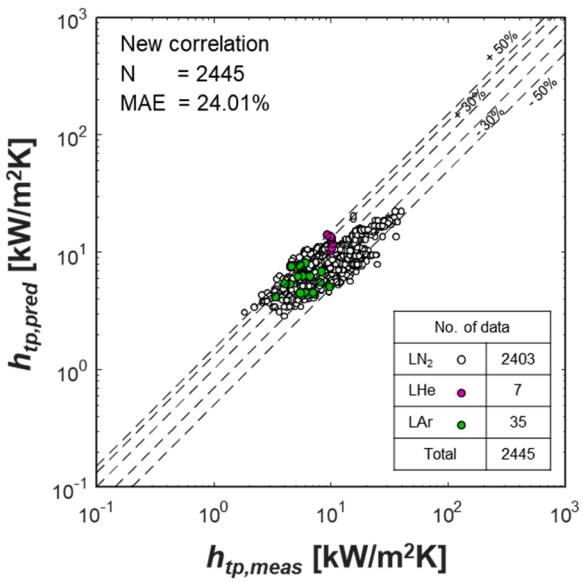

Fig. 13. Performance of the new saturated flow boiling HTC correlation against 1-g_e saturated HTC data for three different cryogens, LN_2, LHe, and LAr.

micro-channel array heat sinks [65], and nPFH flow boiling for in-space thermal management [33]. This suggests that the dimensionless groups incorporated into Moles and Shaw's correlation formulation effectively account for the underlying physical mechanisms at play in subcooled flow boiling. Building upon these findings, the performance of three different categories of correlations is assessed against the demarcated LN_2 subcooled HTC database. The predictive accuracy of each correlation is assessed by evaluating MAE which is defined for local HTC per Eq. (12). The overall MAE of each correlation will be used to determine the most accurate correlation for the database.

4.2.2. Assessment results and discussion

Fig. 15 presents parity plots for comprehensive evaluation of the seminal subcooled flow boiling correlations. Among these, the correlation by Devahdhanush and Mudawar [33] emerges as the top performer, exhibiting a MAE value of 29.83 %, with the majority of datapoints exhibiting predictions that closely align with the 45° diagonal line and

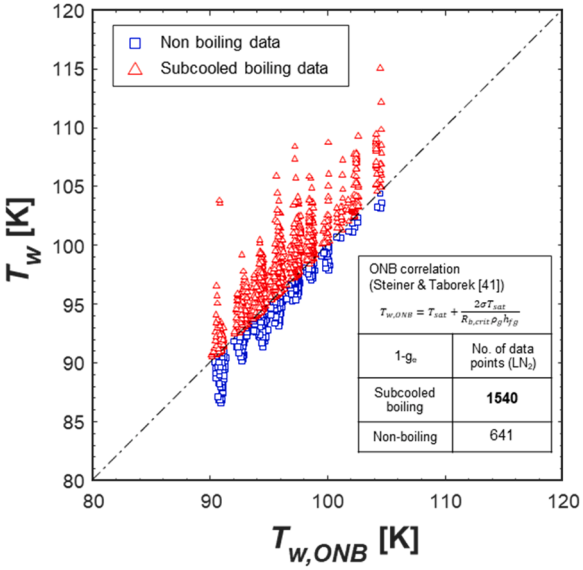

Fig. 14. Data demarcation based on ONB correlation by Steiner and Taborek [41].

Table 5
Prior seminal subcooled HTC correlations.

Author(s)	Correlation	Remarks
Papell [28]	$\frac{Nu_{sc}}{Nu_{sp}} = 90\left(\frac{q''_w}{h_{fg}\rho_g U}\right)^{0.7}\left(\frac{h_{fg}}{c_{p,f}\Delta T_{sub}}\right)^{0.84}\left(\frac{\rho_g}{\rho_f}\right)^{0.756}$ $= 90Bo^{0.7}Ja^{**-0.84}(\rho_g/\rho_f)^{0.756}$ $Nu_{sp} = 0.021Re_f^{0.8}Pr_f^{0.4}$	• Fluids: distilled water, ammonia • Single-phase heat transfer coefficient is calculated using a Colburn-type equation [66] with properties evaluated at film temperature
Moles and Shaw [31]	$\frac{Nu_{sc}}{Nu_{sp}} = 78.5\left(\frac{q''_w}{h_{fg}\rho_g U}\right)^{0.67}\left(\frac{h_{fg}}{c_{p,f}\Delta T_{sub}}\right)^{0.5}\left(\frac{\rho_g}{\rho_f}\right)^{0.7}\left(\frac{c_{p,f}\mu_f}{k_f}\right)^{0.46}$ $= 78.5Bo^{0.67}Ja^{**-0.5}(\rho_g/\rho_f)^{0.03}Pr_f^{0.46}$ $Nu_{sp} = 0.027Re_f^{0.8}Pr_f^{1/3}\left(\frac{\mu_f}{\mu_f\vert_{T_w}}\right)$	• Flow orientation: vertical upflow, horizontal flow • Fluids: water, ethanol, isopropanol, n-butanol, ammonia, aniline, hydrazine • Single-phase heat transfer coefficient is calculated using Sieder-Tate's equation [67]
Liu and Winterton [36]	$q''_w = ((Eh_{sp}(T_w - T_f))^2 + (Sh_{nb}\Delta T_{sat})^2)^{0.5} = h_{sc}(T_w - T_f)$ $h_{sc} = \left((Eh_{sp})^2 + \left(\frac{Sh_{nb}\Delta T_{sat}}{T_w - T_f}\right)^2\right)^{0.5}$ $Nu_{sp} = 0.023Re_{fo}^{0.8}Pr_f^{0.4}$ $h_{NB} = 55P_R^{0.12}(-\log_{10}P_R)^{-0.55}q^{2/3}M^{-0.5}$ For vertical flow, $E_{NB} = E_{CB} = 1$ For horizontal flow, if $Fr_{fo,D} \geq 0.05$, $E = 1$ if $Fr_{fo,D} < 0.05$, $E = Fr_{fo,D}^{(}0.1 - 2Fr_{fo,D})$ $S = Fr_{fo,D}^{0.5}$	• Flow orientation: vertical upflow, vertical downflow, horizontal flow • Fluids: water, R11, R12, R113, R114, R22, ethylene glycol, n-butanol, ethanol • Single-phase heat transfer coefficient is calculated using Dittus-Boelter's equation [68]
Shah [38]	$q''_w = h_{sc}(T_w - T_f) =$ $\{\frac{\psi_0 h_{sp}(\Delta T_{sat} - 1.65\Delta T_{sub}^{-0.44})}{0.67}PDB\psi_0 h_{sp}\Delta T_{sat}FDB$ $\psi_0 = \begin{cases} 230Bo^{0.5} & Bo > 0.3\times10^{-4} \\ 1 + 46Bo^{0.5} & Bo < 0.3\times10^{-4} \end{cases}$ $Nu_{sp} = 0.023Re_f^{0.8}Pr_f^{0.4}$	• Flow orientation: vertical upflow, horizontal flow • Fluids: 13 different fluids (water, refrigerants, chemicals) • Single-phase heat transfer coefficient is calculated using Dittus-Boelter's equation [68]
Devahdhanush and Mudawar [33]	$\frac{Nu_{sc}}{Nu_{sp}} = 312.8\left(\frac{q''_w}{Gh_{fg}}\right)^{0.769}\left(0.1 + \frac{c_{p,f}\Delta T_{sub}}{h_{fg}}\right)^{-0.632}$ $= 312.8Bo^{0.769}(0.1 + Ja^{**})^{-0.632}$ $Nu_{sp} = 0.023Re_{fo}^{0.8}Pr_f^{0.4}$	• Flow orientation: vertical upflow, vertical downflow, horizontal flow • Fluids: n-Perfluorohexane (nPFH) • Single-phase heat transfer coefficient is calculated using Dittus-Boelter's equation [68] with all properties based on local bulk fluid temperature and liquid-only Reynolds number

falling within the ±50 % boundaries. Devahdhanush and Mudawar's correlation belongs to the dimensionless-group-type correlation alongside the correlations by Papell [28] and Moles and Shaw [31], which yielded MAE values of 467.54 % and 86.83 %, respectively. Unlike Devahdhanush and Mudawar's correlation, these correlations tend to overpredict the local subcooled HTC for the demarcated LN_2 subcooled HTC data, and this overprediction becomes more pronounced as HTC values increase. The substantial disparities observed from the correlations by Papell and Moles and Shaw can be attributed to the fact that these correlations contain a ΔT_{sub} parameter raised to a negative power, which leads to worsening predictions as $x_e \rightarrow 0$. This issue relates to numerical divergence of the functional form involving modified Jacob number, Ja^{**}, and its corresponding remedy will be further elaborated in the following section. The superposition-type correlation developed by Liu and Winterton [36] demonstrates moderate accuracy with an MAE of 37.80 %. This correlation is developed based on Chen's correlation [39] for saturated flow boiling and incorporates auxiliary correlations for liquid convection (Dittus-Boelter [68]) and nucleate pool boiling (Cooper [59]), but with modified enhancement and suppression factors. While this correlation is developed based on consolidated databases encompassing various fluids flowing in both vertical and horizontal orientations, it tends to overpredict for the present database, with only a small subset of datapoints falling within the ±50 % error band. Shah's correlation [38] requires datapoints to be demarcated into PDB and FDB based on his own empirically-derived criterion. As shown in Fig. 15, this correlation results in moderate accuracy of MAE of 39.01 %, but only slightly misaligned to the 45° diagonal line, which might be caused by improperly regressed empirical constants for the present dataset. Evaluation statistics against the final demarcated subcooled HTC database are comprehensively summarized in Table 6.

4.2.3. Numerical divergence issue and remedy to use Jacob number

Fig. 16 presents a plot of $h_{sc,pred}/h_{sc,meas}$ versus local quality for the dimensionless-group-type correlations of Papell [28], Moles and Shaw [31], and Devahdhanush and Mudawar [33]. Validating the assessment results of the previous section, in Fig. 16, the majority of datapoints are predicted within the ±30 % boundaries using Devahdhanush and Mudawar's correlation, with almost no overpredictions. In contrast, when employed with Papell's and Moles and Shaw's correlations, the predicted datapoints exhibit substantial overprediction as x_e approaches zero. Indeed, this issue is purely a numerical divergence problem stemming from the inversion of the modified Jacob number term, which introduces an artificial singularity at $\Delta T_{sub} = 0$. The degree of divergence observed in Papell's correlation is notably higher, primarily due to the larger power of 0.84 applied to the inverse Jacob number, compared to the value of 0.5 used in Moles and Shaw's correlation. As a remedy to remove the singularity as $\Delta T_{sub} \rightarrow 0$, Devahdhanush and Mudawar [33] proposed using $(0.1 + Ja^{**})$, instead of Ja^{**}. They reported that a value of 0.1 ensures that the added constant does not overshadow the effects of subcooling and preserves physical trends. Based on the success of the Devahdhanush and Mudawar's correlation, the proposed $(0.1 + Ja^{**})$ term will also be employed in the new subcooled HTC correlation.

4.3. New subcooled HTC correlation

4.3.1. New correlation and its statistics

Based on the assessment results of the seminal correlations, heat transfer enhancement provided by subcooled boiling over pure liquid convection, h_{sc}/h_{sp}, is expected to have the following functional form,

$$\frac{h_{sc}}{h_{sp}} = C_1\left(\frac{q''}{Gh_{fg}}\right)^{C_2}\left(0.1 + \frac{c_{p,f}\Delta T_{sub}}{h_{fg}}\right)^{C_3}\left(\frac{\rho_g}{\rho_f}\right)^{C_4}\left(\frac{c_{p,f}\mu_f}{k_f}\right)^{C_5} \quad (22)$$

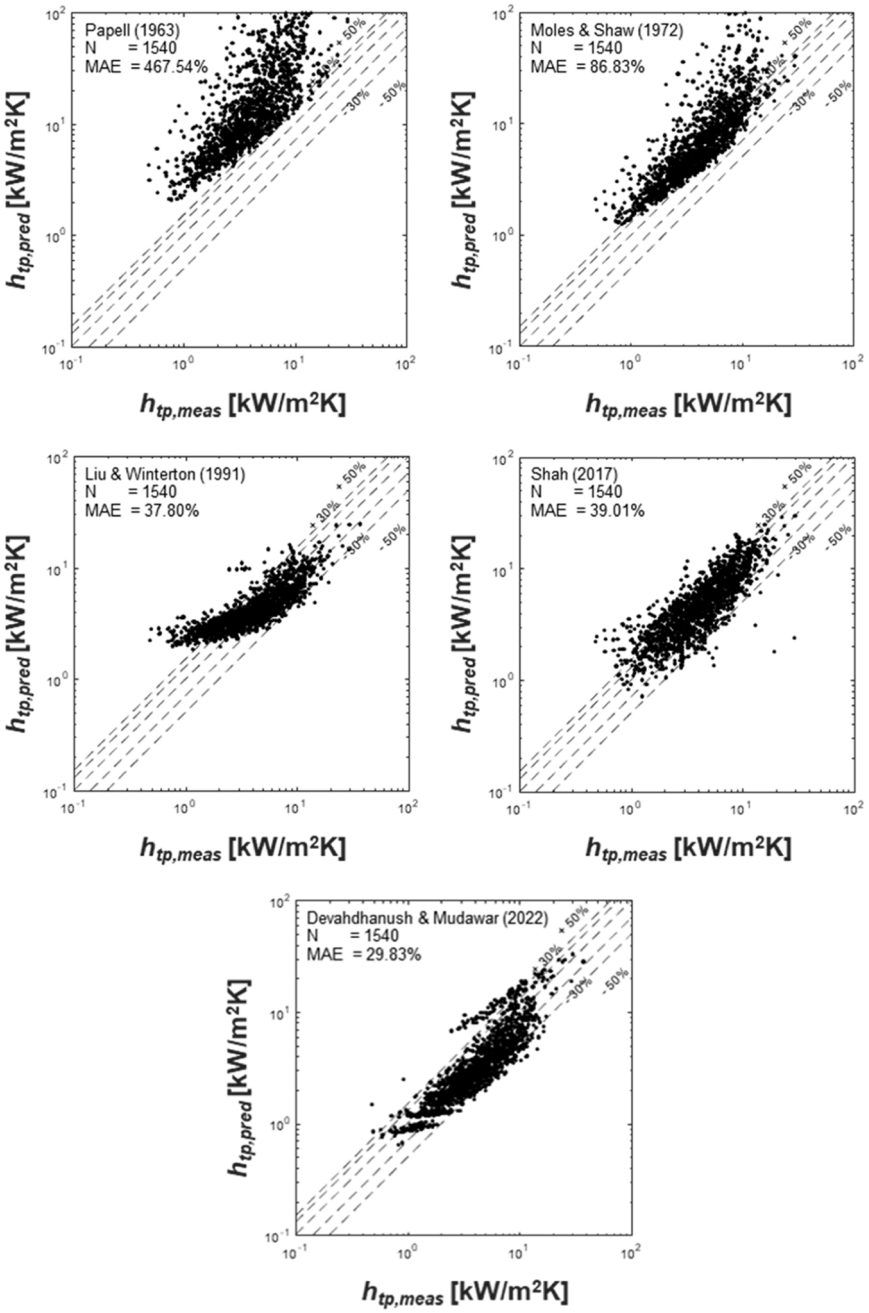

Fig. 15. Performance of seminal subcooled flow boiling HTC correlations against demarcated subcooled HTC data for LN_2 under terrestrial gravity.

Table 6
Prediction statistics for seminal HTC correlations and the new correlation for subcooled flow boiling regime.

Dataset		*N*	New Subcooled correlation *MAE* [%]	Papell (1963) *MAE* [%]	Moles & Shaw (1972) *MAE* [%]	Liu & Winterton (1991) *MAE* [%]	Shah (2017) *MAE* [%]	Devahdhanush & Mudawar (2022) *MAE* [%]
LN_2 Only	Entire 1-g_e dataset	1540	21.24	467.54	86.83	37.80	39.01	29.83
	Microgravity	102	25.99	266.33	53.05	29.76	34.68	28.53
LN_2 LCH_4 LH_2	Entire 1-g_e dataset	1553	21.29	464.55	86.45	37.83	39.87	29.88

where all thermophysical properties are estimated based on local pressure (i.e., local saturation temperature). For uniformity between saturated and subcooled HTC correlations, single-phase liquid HTC, h_{sp}, by Gnielinski [62] is selected and incorporated in the new correlation. Boiling number and modified Jacob number, the two terms that mostly affect heat transfer enhancement and are consistent in all seminal dimensionless-group correlations, are included. To remove the singularity as $\Delta T_{sub} \rightarrow 0$, $(0.1 + Ja^{**})$ is employed, instead of Ja^{**}. In order to

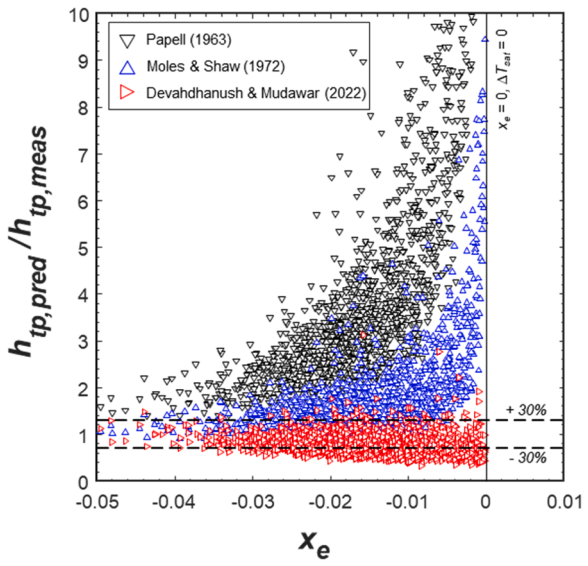

Fig. 16. $h_{tp,pred}/h_{tp,meas}$ ratio versus thermodynamic equilibrium quality for three different seminal correlations [28,31,33] against demarcated subcooled HTC data for LN_2.

address thermal properties of different cryogens, dimensionless group of vapor-to-liquid density ratio and liquid Prandtl number are retained, based on successful coverage of Moles and Shaw's correlation for a wide variety of fluid classes. Note that the suggested functional form does not reflect any gravity effect on subcooled HTC. This is based on the observed trend from the experimental database, where a significant impact of the reduced gravity field on subcooled HTC cannot be identified. The final correlation for LN_2 subcooled HTC is

$$\begin{aligned}\frac{h_{sc}}{h_{sp}} &= 6.58\left(\frac{q''}{Gh_{fg}}\right)^{0.68}\left(0.1+\frac{c_{p,f}\Delta T_{sub}}{h_{fg}}\right)^{-1.3}\left(\frac{\rho_g}{\rho_f}\right)^{-0.4}\left(\frac{c_{p,f}\mu_f}{k_f}\right)^{0.46} \\ &= 6.58Bo^{0.68}(0.1+Ja^{**})^{-1.3}\left(\frac{\rho_g}{\rho_f}\right)^{-0.4}(Pr_f)^{0.46}\end{aligned} \tag{23}$$

where the constants are regressed with an aim of minimizing the predictive error (the numerical regression is made certain to find the global minima within the expected ranges), while preserving physical trends. The predictive performance of the newly developed correlation over the final demarcated LN_2 saturated HTC database is thoroughly presented, both statistically in Table 6 and visually in Fig. 17. In Fig. 17(a), the parity plot shows the alignment of the local HTC datapoints along the 45° diagonal line and within ±50 % boundaries, resulting in an overall MAE of 21.24 % for the terrestrial gravity condition. Fig. 17(b) further highlights the predictive capability of this new correlation, showcasing an overall MAE of 25.99 % for microgravity conditions. The superiority of the new subcooled HTC correlation is also evident in Table 6, where this correlation excels as the best-performing for both the terrestrial 1-g_e LN_2 database and the microgravity LN_2 database. In light of the comprehensive evaluation and analysis presented, it is clear that the newly developed correlation offers robust predictive accuracy across a wide spectrum of operating conditions, flow orientations, and across a broad range of gravity levels for LN_2.

4.3.2. Extension of the new correlation to other cryogens

In order to assess the universality of the correlation, an evaluation was conducted utilizing local subcooled HTC datapoints obtained for different cryogenic fluids. Rigorous application of the segregation criteria, with $D > 6.35$ mm, resulted in the demarcation of 1553 local subcooled HTC datapoints, encompassing three distinct cryogens: liquid nitrogen (LN_2), liquid methane (LCH_4), and liquid hydrogen (LH_2). In contrast to the new saturated HTC correlation, which exhibited robust

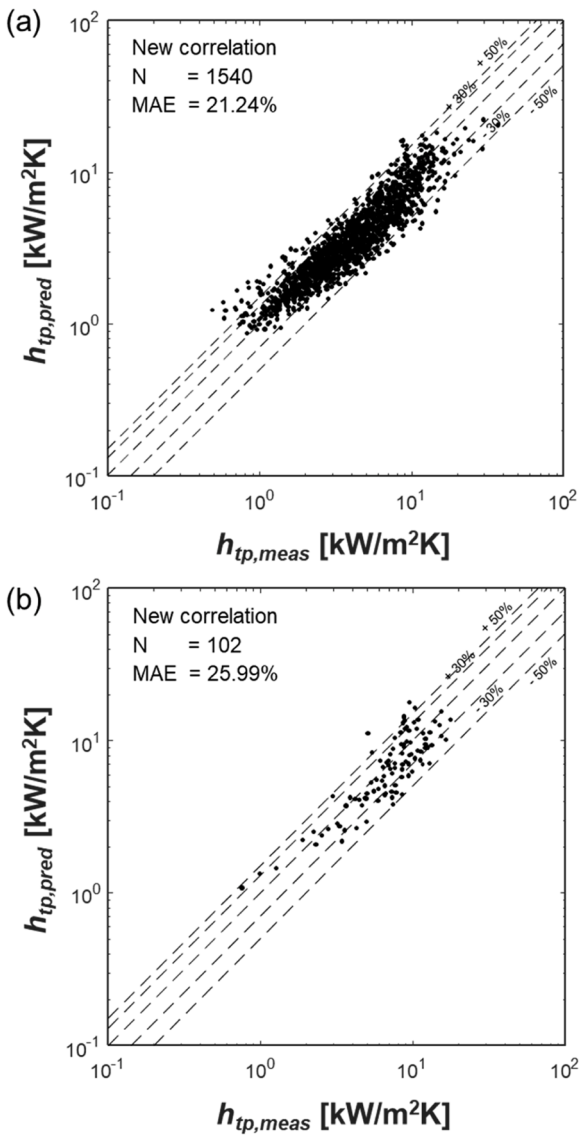

Fig. 17. Performance of the new subcooled flow boiling HTC correlation against the demarcated (a) 1-g_e subcooled HTC data for LN_2, and (b) μg subcooled HTC data for LN_2.

predictive capability across different cryogens without any modifications, the new subcooled HTC correlation for LN_2, Eq. (23), necessitated the incorporation of an additional term to achieve improved accuracy in representing subcooled HTC for other cryogens. To account for the distinct characteristics of different cryogenic fluids, a simple, yet powerful correction factor based on molecular weight ratio (ratio of the molecular weight of LN_2 to the molecular weight of the specific cryogen) is proposed,

$$\frac{h_{sc}}{h_{sc,LN_2}} = \left(\frac{\bar{M}_{LN2}}{\bar{M}}\right)^m \tag{24}$$

The impact of molecular weight on the heat transfer coefficient has been proposed by Cooper [69] based on empirical observations of experimental data, without providing a specific theoretical explanation for the observed relationship. In Cooper's pool boiling HTC correlation [59], he suggested inverse proportionality between h_{PB} and $\bar{M}$, and postulated a functional relation of the form $h_{PB} \sim \bar{M}^{-0.5}$. This inverse proportionality has also been observed within the current subcooled HTC database for cryogens. To gain a theoretical understanding of the experimentally observed relationship between the two-phase heat

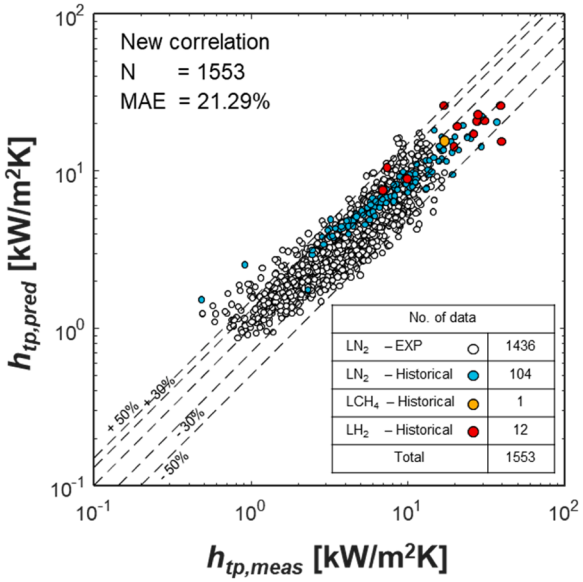

Fig. 18. Performance of the new subcooled flow boiling HTC correlation against *1-g_e* saturated HTC data for three different cryogens, LN_2, LCH_4, and LH_2.

transfer coefficient, h_{tp}, and molecular weight, $\bar{M}$, bubble nucleation theory and kinetic theory of gases were employed to derive a theoretical functional relationship. A detailed derivation of the theoretical functional relationship can be found in *Appendix A*. The analysis, both qualitatively and quantitatively, validates the need for the additional term presented in Eq. (24). It should be noted that Eq. (24) is non-dimensionalized by incorporating the molecular weight of LN_2, $\bar{M}_{LN2}$.

Hence, the universal subcooled HTC correlation can be expressed using Eqs. (23) and (24). Additional regression analysis for the power factor, m, yields

$$\frac{h_{sc}}{h_{sp}} = 6.58\left(\frac{q''}{Gh_{fg}}\right)^{0.68}\left(0.1+\frac{c_{p,f}\Delta T_{sub}}{h_{fg}}\right)^{-1.3}\left(\frac{\rho_g}{\rho_f}\right)^{-0.4}\left(\frac{c_{p,f}\mu_f}{k_f}\right)^{0.46}\left(\frac{\bar{M}_{LN2}}{\bar{M}}\right)^{0.42}$$
$$= 6.58Bo^{0.68}(0.1+Ja^{**})^{-1.3}\left(\frac{\rho_g}{\rho_f}\right)^{-0.4}(Pr_f)^{0.46}\left(\frac{\bar{M}_{LN2}}{\bar{M}}\right)^{0.42} \quad (25)$$

As depicted in Fig. 18, the new universal subcooled HTC correlation exhibits an overall MAE of 21.29 % against the entire subcooled HTC database, as also listed in Table 6. This finding underscores the universal applicability of the newly established correlation, extending its effectiveness not only to LN_2 but also to other cryogenic fluids.

5. Conclusions

The present study was motivated by the absence of reliable, error-free saturated and subcooled flow boiling HTC correlations which are essential needs for future cryogenic space applications. Databases for saturated and subcooled HTC were consolidated including experimental data from previous studies of the present authors and historical data extracted from open literatures. Based on the consolidated databases, new HTC correlations were developed and validated for reliability and applicability across a comprehensive range of operating conditions, flow orientations, and cryogenic fluids. Key conclusions from the study are:

(1) Assessment of prior seminal saturated HTC correlations for the terrestrial LN_2 saturated database revealed predictive MAEs ranging from 28.89 % to 52.44 %. Amongst all, Ganesan et al.'s [27] performed the best, with an overall MAE of 28.89 %. However, for the microgravity dataset, Ganesan et al.'s resulted in an overall MAE of 52.59 %, leaving no viable saturated HTC correlation applicable to both 1-g_e and microgravity.

(2) A new saturated HTC correlation was proposed based on comprehensive analysis of the suggested functional form, addressing the effects of suppression of nucleate boiling, gravitational effects on nucleate boiling, and reliance of convection boiling on the phase separation parameter. The overall MAEs for the new saturated HTC correlation are 23.84 % and 16.73 % for 1-g_e and microgravity saturated HTC, respectively. The correlation was further assessed against multiple cryogens under terrestrial gravity condition and proved its universality with an overall MAE of 24.01 %.

(3) Assessment of prior seminal subcooled correlations for the terrestrial LN_2 subcooled database showed MAEs ranging from 29.83 % to 467.54 %. Amongst all, Devahdhanush and Mudawar's [33] performed the best, with an overall MAE of 29.83 %.

(4) A simple to use, but highly effective correlation of the dimensionless group type was developed for cryogenic subcooled flow boiling. The overall MAEs of the new subcooled HTC correlation are 21.24 % and 25.99 %, for 1-g_e and microgravity, respectively. The correlation incorporates a correction factor based on molecular weight ratio and was further assessed against multiple cryogens under terrestrial gravity condition and validated for universal applicability with an overall MAE of 21.29 %.

(5) Clearly, the new saturated and subcooled HTC correlations outperform all prior seminal correlations, consistently providing excellent predictions for both terrestrial gravity and microgravity conditions, as summarized in Tables 4 and 6. The new HTC correlations can be utilized irrespective of flow orientation and gravity level for various cryogenic fluids.

Author declaration

We wish to confirm that there are no known conflicts of interest associated with this publication and there has been no significant financial support for this work that could have influenced its outcome.

We confirm that the manuscript has been read and approved by all named authors and that there are no other persons who satisfied the criteria for authorship but are not listed. We further confirm that the order of authors listed in the manuscript has been approved by all of us.

We confirm that we have given due consideration to the protection of intellectual property associated with this work and that there are no impediments to publication, including the timing of publication, with respect to intellectual property. In so doing we confirm that we have followed the regulations of our institutions concerning intellectual property.

We understand that the Corresponding Author is the sole contact for the Editorial process (including Editorial Manager and direct communications with the office). He/she is responsible for communicating with the other authors about progress, submissions of revisions and final approval of proofs. We confirm that we have provided a current, correct email address which is accessible by the Corresponding Author and which has been configured to accept email from mudawar@ecn.purdue.edu

CRediT authorship contribution statement

Sunjae Kim: Conceptualization, Data curation, Formal analysis, Investigation, Methodology, Software, Validation, Writing – original draft, Writing – review & editing. **Steven J Darges:** Conceptualization, Formal analysis, Investigation, Methodology. **Jason Hartwig:** Conceptualization, Methodology, Project administration, Supervision, Writing – review & editing. **Issam Mudawar:** Funding acquisition, Investigation, Methodology, Project administration, Resources, Supervision, Writing – original draft, Writing – review & editing.

Declaration of competing interest

The authors declare the following financial interests/personal relationships which may be considered as potential competing interests:

Issam Mudawar reports financial support was provided by NASA. If there are other authors, they declare that they have no known competing financial interests or personal relationships that could have appeared to influence the work reported in this paper.

Data availability

The data that has been used is confidential.

Acknowledgement

The authors are appreciative of the support of the National Aeronautics and Space Administration (NASA) under grants 80NSSC21K0500 and 80GRC018C0055. The authors thank previous PU-BTPFL members Raj Patel and Vishwanath Ganesan for their efforts in extracting HTC data from various literature sources.

Appendix A

As discussed earlier, formulation of the new correlation for subcooled HTC for cryogens was shown to include dependence on molecular weight, $\bar{M}$. This Appendix is intended to provide a theoretical basis for this relationship.

A.1 Bubble nucleation

A.1.1 Metastable superheated liquid

To initiate the discussion on bubble nucleation, it is crucial to grasp the concept of metastable state of a vapor embryo, with the goal of determining whether such an embryo can maintain a stable state and continue to grow through phase change. Consider a scenario where a superheated pure substance liquid bath exists at T_f and P_f, within which a spherical vapor bubble embryo with a radius r is present. Relying on the definition of the availability function, Ψ, in Eq. (A1), which is derived from the Kelvin equation, the availability of the liquid, vapor embryo, and interface can be defined according to Eq. (A2).

$$\Psi = U - TS + PV \tag{A1}$$

$$\Psi = \Psi_f + \Psi_g + \Psi_i \tag{A2}$$

where U, S, and V represent internal energy, entropy, and volume, respectively. Defining the availability for liquid, interface, and vapor as Eqs. (A3)–(A5), respectively, and employing the relation in Eq. (A6), the total availability of the embryo can be expressed as Eq. (A7).

$$\Psi_f = m_f\left(U_f - T_f S_f + P_f V_f\right) \tag{A3}$$

$$\Psi_i = 4\pi r 2\sigma \tag{A4}$$

$$\Psi_g = m_g\left(U_g - T_f S_g + P_f V_g\right) \tag{A5}$$

$$\Delta\Psi = \Psi_f + \Psi_g + \Psi_i - \Psi_0 \tag{A6}$$

$$\Delta\Psi = m_g\left[g_g\left(T_f, P_f\right) - g_f\left(T_f, P_f\right) + \left(P_f - P_g\right)\right] + 4\pi r 2\sigma \tag{A7}$$

where m_f, m_g, g_g, and g_f are mass of a liquid molecule, mass of a vapor molecule, specific Gibbs function for liquid, and specific Gibbs function for vapor, respectively. Replacing the term $(P_f - P_g)$ in Eq. (A7) with the Young-Laplace relation $P_g = P_{ge} = P_f - 2\sigma/r_e$, yields

$$\Delta\Psi = m_g\left[g_g\left(T_f, P_f\right) - g_f\left(T_f, P_f\right) - \frac{2\sigma v_g}{r_e}\right] + 4\pi r 2\sigma \tag{A8}$$

where P_{ge} and r_e are pressure of vapor embryo at equilibrium, and radius of vapor embryo at equilibrium, respectively. For pure substances, Gibbs free energies for vapor and liquid are identical. Therefore, g_g and g_f cancel out and, by incorporating mass and volume of vapor, m_g, and v_g, respectively, Eq. (A8) can be simplified into the following expression for availability of an embryo of any radius r.

$$\Delta\Psi = 4\pi r 2\sigma\left[1 - \frac{2}{3}(r/r_e)\right] \tag{A9}$$

It is clear that the condition described by Eq. (A9) leads to a state of metastable equilibrium rather than stable equilibrium. In this state, the removal of a molecule from the activated embryo cluster with a radius r_e results in its collapse, while the addition of a molecule leads to spontaneous growth, i.e., homogenous bubble nucleation [70].

A.1.2 Rate of bubble formation, J

Drawing upon the stability analysis presented above, it is evident that homogeneous nucleation hinges on the net difference between the rates of interfacial evaporation and condensation. The rate of bubble formation per unit volume per unit time, J, was derived for both homogeneous and heterogenous nucleation by Blander and Katz [71], and their formulation is summarized herein.

Let's consider a pure substance superheated liquid bath at T_f and P_f, where an idealized distribution of vapor embryos exists within the liquid bath. The number of embryos of n molecules per unit volume, N_n, for such equilibrium system can be postulated to have the form

$$N_n = N_f \ exp\left(\frac{-\Delta\Psi(r)}{K_B T_f}\right) \tag{A10}$$

where the prefactor N_f is defined as the number of the liquid molecules per unit volume, and K_B is the Boltzmann constant ($=\bar{R}\ /N_{A,}$), $\bar{R}$ and N_A being the universal gas constant and Avogadro's number, respectively. For equilibrium, Eq. (A11) below must be satisfied, indicating dynamic equilibrium between total number of evaporating molecules and total number of condensing molecules.

$$N_n A_n j_{ne} = N_{n+1} A_{n+1}\ j_{(n+1)c} \tag{A11}$$

where j_{ne} is defined as the number of molecules evaporating from the interface per unit area per unit time, and j_{nc} is the number of molecules condensing along the interface per unit area per unit time. Eq. (A11) indicates the dynamic equilibrium describing the condition where the rate at which embryos with n molecules are converted to embryos with $n + 1$ molecules by evaporation is equal to the rate at which embryos with $n + 1$ molecules are converted to embryos with n molecules by condensation.

However, for a real superheated liquid, ideal equilibrium cannot be expected and the difference between the evaporation and condensation rates will represent the net flux of the number of embryos. Therefore, J_n denotes the excess number of embryos with n molecules being converted to $n + 1$ by evaporation over the number of embryos with $n + 1$ molecules being converted to n by condensation, as represented in Eq. (A12). Here, N_n^* denotes the number of embryos in this non-equilibrium situation. Combining Eqs. (A11) and (A12) yields Eq. (A13).

$$J_n = N_n^* A_n j_{ne} - N_{n+1}^*\ A_{n+1}\ j_{(n+1)c} \tag{A12}$$

$$J_n = N_n A_n j_{ne}\left[\frac{N_n^*}{N_n} - \frac{N_{n+1}^*}{N_{n+1}}\right] \tag{A13}$$

By treating the number of molecules in the embryo, n, as a continuous variable, Eq. (A13) can be expressed as Eq. (A14). Furthermore, by assuming constant number distribution of embryo ($\partial N_n^*/\partial t = 0$), it yields Eq. (A15), which indicates the rate of bubble formation is independent of embryo size n.

$$J_n = -N_n A_n j_{ne}\frac{\partial\left[N_n^*/N_n\right]}{\partial n} \tag{A14}$$

$$\frac{\partial N_n^*}{\partial t} = \frac{\partial J_n}{\partial n} = 0 \rightarrow J_n = J \tag{A15}$$

Integrating Eq. (A14) over the size distribution from n_0 to n, and with $\frac{N_n^*}{N_n} \rightarrow 1$ for small n, yields Eq. (A16).

$$J = \frac{N_n^*}{N_n}\cdot\left[\int_{n=n}^{n=n_0}\left[N_n A_n j_{ne}\right]^{-1} dn\right]^{-1} = \left[\int_{n=n}^{n=n_0}\left[N_n A_n j_{ne}\right]^{-1} dn\right]^{-1} \tag{A16}$$

Note that the trend of N_n^* can be found in [70].

According to Schrage et al. [72], the number of molecules evaporating from the interface, j_{ne}, can be expressed as Eq. (A17), the derivation of which will be discussed in detail in the following section.

$$j_{ne} = \frac{P_{ge}}{\left(2\pi m k_B T_f\right)^{1/2}} \tag{A17}$$

By substituting Eqs. (A17) into (A16), and incorporating the Young-Laplace equation, the integration relation in Eq. (A16) can be re-expressed as a function of r.

$$J = \left[\frac{3N_f}{2 - P_f/P_{ge}}\right]\cdot\left[\frac{K_B T_f}{2\pi m}\right]^{1/2}\cdot\left[\int_0^{\infty} exp\left(\frac{\Delta\Psi(r)}{K_B T_f}\right) dr\right] \tag{A18}$$

Substituting the relation for $\Delta\Psi(r)$, Eq. (A9), into (A18) yields the following relation for J:

$$J = N_f\left[\frac{3\sigma}{\pi m}\right]^{1/2}\cdot exp\left[\frac{-16\pi\sigma^3}{3kT\left[P_{ge} - P_f\right]^2}\right] \tag{A19}$$

Expressing Eq. (A19) by substituting the known constants, results in

$$J = 1.44\left(10^{40}\right)\cdot\left[\frac{{\rho_f}^2\sigma}{\bar{M}^3}\right]^{1/2}\cdot exp\left[\frac{-1.213\left(10^{24}\right)\sigma^3}{T\left[\eta P_{sat} - P_f\right]^2}\right] \tag{A20}$$

In Eq. (A20) shows the rate of bubble formation, J, is related to molecular weight, $\bar{M}$, according $J \sim \bar{M}^{-3/2}$. The inverse proportionality relation indicates a reduced likelihood of bubble nucleation for substances with high molecular weight. Conversely, it also suggests a heightened probability of bubble nucleation for substances with low molecular weight. Consequently, Eq. (A20), provides qualitative insight into the influence of molecular weight on interfacial heat transfer, which is predominantly affected by the rate of bubble formation, J.

A.1.3 Heterogenous nucleation

For heterogeneous nucleation, straightforward extension of the previous analysis for homogeneous nucleation can be realized. The key factor that remains to be considered is the influence of cavities on the heated surface, which can vary depending on the geometry of each cavity. Cole [73] evaluated and provided functional relationships for various geometries, including flat surfaces, spherical projections, spherical cavities, and conical cavities. By incorporating these functional relations, Eq. (A19) can be redefined to account for heterogeneous nucleation according to

$$J = {N_f}^{2/3} Y \left[\frac{3\sigma}{C\pi m}\right]^{1/2} \cdot exp\left[\frac{-16\pi\sigma^3 C}{3kT\left[P_{ge} - P_f\right]^2}\right] \tag{A21}$$

where m is mass of a single molecule and C and Y are Cole's geometrical relations, defined as $C = (2+3cos\theta - cos^3\theta)/4$ and $Y = (1 + cos\theta)/2$, respectively. Note that the relation for C is derived for vapor embryo on a plane surface with a contact angle of θ. Notice the smaller prefactor, ${N_f}^{2/3}$, than that for the homogenous case, Eq. (A19). For heterogeneous nucleation, only the liquid molecules in close proximity to the solid surface are involved in the formation of embryo bubbles. As a result, the exponential term for the prefactor is 2/3, in contrast to the value of 1 used for homogeneous nucleation. Nevertheless, by substituting the known constants, an inverse proportionality functional relationship is realized between the rate of heterogeneous bubble formation and molecular weight, as $J \sim \bar{M}^{-7/6}$, which indicates a dependence of heat transfer on molecular weight similar to the homogeneous bubble nucleation case. Notice that if θ is assumed to be zero and ${N_f}^{2/3}$ is replaced by N_f, Eq. (A21) becomes identical to Eq. (A19) for homogeneous bubble nucleation.

A.2 Molecular dynamics and interfacial heat and mass transfer

While a *qualitative* understanding of the relationship between molecular weight and interfacial heat transfer was provided above, it is essential to develop a *quantitative* representation of this relationship for the purpose of developing a HTC correlation that incorporates the molecular weight effect. To meet this requirement, interfacial evaporation and condensation should be investigated at the molecular scale, focusing on the proximity of the liquid-vapor interface.

A.2.1 Kinetic theory of gases

According to the classical kinematic theory of gases, Maxwell velocity distribution, Eq. (A22), dictates the fraction of the total number of molecules, n, with Cartesian velocity u, v, and w in the ranges of u+du, v+dv, and w+dw, respectively [74].

$$\frac{dn_{uvw}}{n} = \left(\frac{m}{2\pi K_B T}\right)^{3/2} \cdot exp\left[-\left(\frac{m}{2K_B T}\right)\left(u^2+v^2+w^2\right)\right] dudvdw \tag{A22}$$

This result can be utilized to determine the flux of molecules passing through an arbitrary surface for a gas that has a Maxwell velocity distribution. First, Eq. (A23) integrates the fraction of molecules having an x-component velocity of u with any v and w to acquire the fraction of molecules that have potential to traverse the arbitrary surface within a given time interval, which can be combined with Eq. (A22) to yield

$$\frac{dn_u}{n} = \int\int \frac{dn_{uvw}}{n} \tag{A23}$$

$$\frac{dn_u}{n} = \left(\frac{m}{2\pi K_B T}\right)^{1/2} exp\left[-\left(\frac{mu^2}{2K_B T}\right)\right] du \tag{A24}$$

Eq. (A24) shows, for a total number of molecule n, the number of molecules with x-component velocity equal to u is dn_u. The actual number of molecules passing through the arbitrary surface with velocity u in the x-direction per unit area per unit time, dj_u, can be expressed as

$$dj_u = \left(\frac{u\Delta t}{L_x}\right) dn_u \left(\frac{1}{L_y L_z}\right)\left(\frac{1}{\Delta t}\right) \tag{A25}$$

where L_x, L_y, and L_z are arbitrary length of imaginary cubical box for each direction, respectively. Finally, by substituting Eq. (A24) for dn_u, Eq. (A25) can be integrated over all possible velocities u from 0 to infinity, yielding the following relation for total rate of molecules passing through the arbitrary surface per unit area,

$$j_n = \left(\frac{1}{4}\right)\left(\frac{n}{V}\right)\left(\frac{8K_B T}{m\pi}\right)^{1/2} = \left(\frac{\bar{M}}{2\pi\bar{R}T}\right)^{1/2}\left(\frac{P}{m}\right) \tag{A26}$$

where V equals the volume of the imaginary box ($= L_x L_y L_z$).

This molecular-level understanding can be extended to phase change situations to quantify the number of molecules crossing the liquid-vapor interface during evaporation or condensation. Notice that Eq. (A26) shares the exact form as Eq. (A17), which describes the number of molecules evaporating from the interface, j_{ne}.

A.2.2 Interfacial heat and mass transfer

The kinetic theory of gases has been extended to phase change processes by Shrage et al. [72]. They demonstrated that when a gas flows perpendicular to a planar surface at a velocity of w_0, the molecular flux through the plane in the direction of the bulk motion can be described by Eq. (A27a) for evaporation and Eq. (A27b) for condensation.

$$j_{nw+} = \Gamma(a)\left(\frac{\bar{M}}{2\pi\bar{R}T}\right)^{1/2}\left(\frac{P}{m}\right) \tag{A27a}$$

$$j_{nw-} = \Gamma(a)\left(\frac{\bar{M}}{2\pi\bar{R}T}\right)^{1/2}\left(\frac{P}{m}\right) \tag{A27b}$$

The prefactor $\Gamma(a)$ takes into account the effect of bulk motion, as defined by Eq. (A28), and is dependent on the argument a, as defined by Eq. (A29) below. Cooper [69] reported correlations between thermal properties such as ρ_g, h_{fg}, k_f, $c_{p,f}$, μ_f and molecular weight $\bar{M}$. Utilizing these relations, the argument a was expressed as a power function of $\bar{M}$, as demonstrated in Eq. (A29). It is important to note that exponent p is introduced to represent the power correlation between interfacial heat flux $q_i^{''}$ and $\bar{M}$. Furthermore, by extracting the reported values of $\Gamma(a)$ from Shrage et al., the function $\Gamma(a)$ in Eq. (A28) was approximated as a function of $\bar{M}$, resulting in the relation $\Gamma(a) \approx exp(1.3/\bar{M}^{p+0.5})$, as represented in Eq. (A28).

$$\Gamma(a) = \exp(a^2) + a\pi^{1/2}[1 + erf(a)] \approx exp\left(\frac{1.3}{\bar{M}^{p+0.5}}\right) \tag{A28}$$

$$a = \frac{w_0}{(2\bar{R}T/\bar{M})^2} = \frac{q_i^{''}}{\rho_g h_{fg}}\left(\frac{2\bar{R}T}{\bar{M}}\right)^{1/2} \approx \left(\frac{1}{\bar{M}}\right)^{p}\left(\frac{1}{\bar{M}}\right)^{1/2} \tag{A29}$$

The net rate of interfacial mass transfer can be evaluated as the difference between evaporation rate and condensation rate. Shrage et al. [72], using Eqs. (A27a) and (A27b), expressed the net interfacial mass transfer rate as

$$m_i^{''} = \left(\frac{\bar{M}}{2\pi\bar{R}}\right)^{1/2}\left(\frac{\Gamma\hat{\sigma}P_g}{T_g^{1/2}} - \frac{\hat{\sigma}P_f}{T_f^{1/2}}\right) \tag{A30}$$

where $\hat{\sigma}$ is a parameter often referred to as accommodation coefficient. By simply multiplying $m_i^{''}$ by the latent heat of vaporization, h_{fg}, the interfacial heat flux, $q_i^{''}$, can be evaluated according to

$$q_i^{''} = m_i^{''}h_{fg} = \left[\left(\frac{\bar{M}}{2\pi\bar{R}}\right)^{1/2}\left(\frac{\Gamma\hat{\sigma}P_g}{T_g^{1/2}} - \frac{\hat{\sigma}P_f}{T_f^{1/2}}\right)\right]\cdot h_{fg} \tag{A31}$$

which can be further represented as a function of $\bar{M}$, according to

$$q_i^{''} \approx \left[(\bar{M})^{\frac{1}{2}}\cdot exp\left(\frac{1.3}{\bar{M}^{p+0.5}}\right)\right]\cdot(\bar{M})^{-1} \tag{A32}$$

Note that $h_{fg} \sim (\bar{M})^{-1}$ is utilized as reported by Cooper [69].

The interfacial heat transfer coefficient, h_i, can be derived by dividing the interfacial heat flux by temperature difference across the interface, as Eq. (A33), which still holds the same functional relation as Eq. (A32) but with the left-hand side as h_i.

$$h_i = \frac{q_i^{''}}{\Delta T} \sim \left[(\bar{M})^{\frac{1}{2}}\cdot exp\left(\frac{1.3}{\bar{M}^{p+0.5}}\right)\right]\cdot(\bar{M})^{-1} \tag{A33}$$

Generalizing this functional form, the relation between h_i and $\bar{M}$ can be represented according to the mathematical form

$$h_i \sim (\bar{M})^{-0.5} exp\left(\frac{1.3}{\bar{M}^{p+0.5}}\right) \tag{A34}$$

By iteratively solving Eqs. (A29) and (A32), convergence is realized with $p \approx 0.45$. Using this value, results from Eq. (A34) are depicted in Fig. A1, which shows h_i decreases with increasing $\bar{M}$. Additionally, the blue curve in Fig. A1 shows LHe and LH_2 are clear outliers among the cryogens, with h_i for LHe more than three times that of LN_2, and h_i for LH_2 more than six times that of LN_2. Therefore, the quantified relationship between interfacial heat transfer and molecular weight just derived aligns well with the qualitative analysis of bubble nucleation presented earlier in Appendix A.1, indicating an inverse proportionality between the two. To incorporate the quantified effect of molecular weight into the new subcooled HTC correlation, a power function is used to closely approximate the relationship in Eq. (A34), emphasizing simplicity and good agreement with the date. Regression of the subcooled HTC data resulted in a function described in Eq. (A35), which is also illustrated by the red curve in Fig. A1, showing a close resemblance to the original function depicted by the blue curve.

$$h_i \sim \left(\frac{1}{\bar{M}}\right)^{0.42} \tag{A35}$$

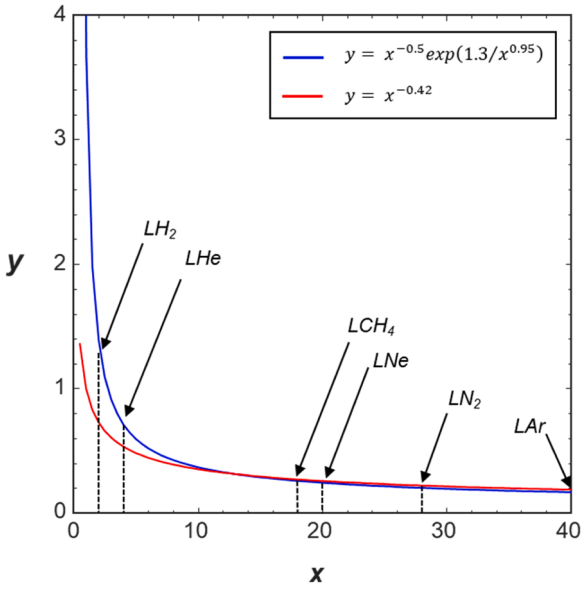

Fig. A1. Generalized functional relationship between interfacial heat transfer coefficient and molecular weight.

References

[1] I. Mudawar, Assessment of high-heat-flux thermal management schemes, IEEE Trans. CPMT 24 (2001) 122–141.
[2] I. Mudawar, Two-phase microchannel heat sinks: theory, applications, and limitations, J. Electron. Packag. Trans. ASME 133 (2011) 041002. -2.
[3] T.J. LaClair, I. Mudawar, Thermal transients in a capillary evaporator prior to the initiation of boiling, Int. J. Heat Mass Transf. 43 (2000) 3937–3952.
[4] S.G. Liter, M. Kaviany, Pool-boiling CHF enhancement by modulated porous-layer coating: theory and experiment, Int. J. Heat Mass Transf. 44 (2001) 4287–4311.
[5] G. Liang, I. Mudawar, Pool boiling critical heat flux (CHF) – part 2: assessment of models and correlations, Int. J. Heat Mass Transf. 117 (2018) 1368–1383.
[6] I. Mudawar, R.A. Houpt, Mass and momentum transport in smooth falling liquid films laminarized at relatively high Reynolds numbers, Int. J. Heat Mass Transf. 36 (1993) 3437–3448.
[7] C.O. Gersey, I. Mudawar, Effects of heater length and orientation on the trigger mechanism for near-saturated flow boiling critical heat flux - II. Critical heat flux model, Int. J. Heat Mass Transf. 38 (1995) 643–654.
[8] S. Mukherjee, I. Mudawar, Pumpless loop for narrow channel and micro-channel boiling from vertical surfaces, J. Electron. Packag. 125 (2003) 431–441.
[9] M.E. Johns, I. Mudawar, An ultra-high power two-phase jet-impingement avionic clamshell module, J. Electron. Packag. 118 (1996) 264–270.
[10] S.N. Joshi, E.M. Dede, Two-phase jet impingement cooling for high heat flux wide band-gap devices using multi-scale porous surfaces, Appl. Therm. Eng. 110 (2017) 10–17.
[11] S. Toda, A study of mist cooling (1st report: investigation of mist cooling), Trans. JSME 38 (1972) 581–588.
[12] W.P. Klinzing, J.C. Rozzi, I. Mudawar, Film and transition boiling correlations for quenching of hot surfaces with water sprays, J. Heat Treat. 9 (1992) 91–103.
[13] L. Lin, R. Ponnappan, Heat transfer characteristics of spray cooling in a closed loop, Int. J. Heat Mass Transf. 46 (2003) 3737–3746.
[14] S. Lee, I. Mudawar, Investigation of flow boiling in large micro-channel heat exchangers in a refrigeration loop for space applications, Int. J. Heat Mass Transf. 97 (2016) 110–129.
[15] S. Lee, V.S. Devahdhanush, I. Mudawar, Pressure drop characteristics of large length-to-diameter two-phase micro-channel heat sinks, Int. J. Heat Mass Transf. 115 (2017) 1258–1275.
[16] M.K. Sung, I. Mudawar, Single-phase and two-phase heat transfer characteristics of low temperature hybrid micro-channel/micro-jet impingement cooling module, Int. J. Heat Mass Transf. 51 (2008) 3882–3895.
[17] M.K. Sung, I. Mudawar, Single-phase and two-phase hybrid cooling scheme for high-heat-flux thermal management of defense electronics, J. Electron. Packag. 131 (2009) 021013.
[18] Y. Li, H. Wu, Experiment investigation on flow boiling heat transfer in a bidirectional counter-flow microchannel heat sink, Int. J. Heat Mass Transf. 187 (2022) 122500.
[19] R. van Erp, R. Soleimanzadeh, L. Nela, G. Kampitsis, E. Matioli, Co-designing electronics with microfluidics for more sustainable cooling, Nature 585 (2020) 211–216.
[20] S. Lee, I. Mudawar, Transient characteristics of flow boiling in large micro-channel heat exchangers, Int. J. Heat Mass Transf. 103 (2016) 186–202.
[21] F.P. Chiaramonte, J. McQuillen, H.K. Nahra, P. Manoharan, H. Vanhala, B.J. Motil, J. Kim, V. Carey, W.G. Anderson, J. Plawsky, L. Carter, A. Jackson, in: Proceedings of the NASA Division of Space and Life and Physical Sciences Research and Applications Fluid Physics Workshop Report, Cleveland, OH, USA, 2020.
[22] W.L. Johnson, J.R. Stephens, NASA's cryogenic fluid management technology development roadmaps, in: Proceedings of the Joint Army-Navy-NASA-Air Force (JANNAF) In-Space Chemical Propulsion Technical Interchange Meeting (TIM), Huntsville, Alabama, USA, 2018.
[23] J. Hartwig, J. Vera, Numerical modeling of the transient chilldown of a cryogenic propellant transfer line, J. Thermophys. Heat Transf. 30 (2016) 1–7.
[24] J. Hartwig, S. Darr, A. Asencio, Assessment of existing two phase heat transfer coefficient and critical heat flux correlations for cryogenic flow boiling in pipe quenching experiments, Int. J. Heat Mass Transf. 93 (2016) 441–463.
[25] M. Meyer, J. Hartwig, S. Sutherlin, A. Colozza, Recent concept study for cryogenic fluid management to support opposition class crewed missions to Mars, Cryogenics 129 (2023) 103622.
[26] M. Mercado, N. Wong, J. Hartwig, Assessment of two-phase heat transfer coefficient and critical heat flux correlations for cryogenic flow boiling in pipe heating experiments, Int. J. Heat Mass Transf. 133 (2019) 295–315.
[27] V. Ganesan, R. Patel, J. Hartwig, I. Mudawar, Review of databases and correlations for saturated flow boiling heat transfer coefficient for cryogens in uniformly heated tubes, and development of new consolidated database and universal correlations, Int. J. Heat Mass Transf. 179 (2021) 121658.
[28] S.S. Papell, Subcooled Boiling Heat Transfer Under Forced Convection in a Heated Tube, Lewis Research Center, Cleveland, OH, USA, 1963. NASA Technical Note D-1583.
[29] M. Badiuzzaman, Correlation of subcooled boiling data, Pak. Eng. 7 (1967) 759–764.
[30] S. Hodgson, PhD Thesis, University of London, London, UK, 1966.
[31] F.D. Moles, J.F.G. Shaw, Boiling heat-transfer to sub-cooled liquids under conditions of forced convection, Trans. Inst. Chem. Eng. 50 (1972) 76–84.
[32] J. Shaw, PhD Thesis, Chemical Engineering, University of Surrey, Guildford, Surrey, UK, 1972.
[33] V.S. Devahdhanush, I. Mudawar, Subcooled flow boiling heat transfer in a partially-heated rectangular channel at different orientations in Earth gravity, Int. J. Heat Mass Transf. 195 (2022) 123200.
[34] R.W. Bjorg, G.R. Hall, W.M. Rohsenow, Correlation of forced convection boiling heat transfer data, Int. J. Heat Mass Transf. 25 (1982) 753–757.
[35] K.E. Gungor, R.H.S. Winterton, A general correlation for flow boiling in tubes and annuli, Int. J. Heat Mass Transf. 29 (1986) 351–358.
[36] Z. Liu, R.H.S. Winterton, A general correlation for saturated and subcooled flow boiling in tubes and annuli, based on a nucleate pool boiling equation, Int. J. Heat Mass Transf. 34 (1991) 2759–2766.
[37] M.M. Shah, A general correlation for heat transfer during subcooled boiling in pipes and annuli, ASHRAE Trans. 83 (1977) 202–217.
[38] M.M. Shah, New correlation for heat transfer during subcooled boiling in plain channels and annuli, Int. J. Therm. Sci. 112 (2017) 358–370.
[39] J.C. Chen, Correlation for boiling heat transfer to saturated fluids in convective flow, Ind. Eng. Chem. Process Des. Dev. 5 (1966) 322–329.
[40] V.V. Klimenko, A generalized correlation for two-phase forced flow heat transfer–second assessment, Int. J. Heat Mass Transf. 33 (1990) 2073–2088.

[41] D. Steiner, J. Taborek, Flow boiling heat transfer in vertical tubes correlated by an asymptotic model, Heat Transf. Eng. 13 (1992) 43–69.
[42] V.E. Schrock, L.M. Grossman, Forced convection boiling in tubes, Nucl. Sci. Eng. 12 (1962) 474–481.
[43] M.M. Shah, Prediction of heat transfer during boiling of cryogenic fluids flowing in tubes, Cryogenics 24 (1984) 231–236.
[44] S.M. Kim, I. Mudawar, Universal approach to predicting saturated flow boiling heat transfer in mini/micro-channels–Part II. Two-phase heat transfer coefficient, Int. J. Heat Mass Transf. 64 (2013) 1239–1256.
[45] S. Kim, N. Damle, J. Hartwig, I. Mudawar, Experimental heat transfer results and flow visualization of horizontal near-saturated liquid nitrogen flow boiling in uniformly heated circular tube under Earth gravity, Appl. Therm. Eng. (2024) in Review.
[46] S. Kim, D. Foster, N. Damle, J. Hartwig, I. Mudawar, Experimental Investigation of flow orientation effects on cryogenic flow boiling, Int. J. Heat Mass Transf. 220 (2024) 124940.
[47] S. Kim, N. Damle, J. Hartwig, I. Mudawar, Cryogenic flow boiling in microgravity: effects of reduced gravity on two-phase fluid physics and heat transfer, Int. J. Heat Mass Transf. 218 (2024) 124751.
[48] E.W. Lemmon, M.L. Huber, M.O. McLinden, NIST standard reference database 23: reference fluid thermodynamic and transport properties-REFPROP, Version 10.0, Gaithersburg, Maryland, USAl, 2018.
[49] T.C. Core, J.F. Harkee, B. Misra, K. Sato, Heat Transfer Studies, Aerojet-General Corporation, USA, 1959. Technical Note WADD-60-239.
[50] J.P. Lewis, J.H. Goodykoontz, J.F. Kline, Boiling heat transfer to liquid hydrogen and nitrogen in forced flow, NASA Technical Note D-1314, USA (1962).
[51] M.R. Glickstein, R.H. Whitesides, Forced-convection nucleate and film boiling of several aliphatic hydrocarbons, in: Proceedings of the ASME-AIChE Heat Transfer Conference and Exhibit 67-HT-7, Seattle, USA, 1967, pp. 1–8.
[52] P.J. Giarratano, R.C. Hess, M.C. Jones, Forced Convection Heat Transfer to Subcritical Helium I, National Bureau of Standards, 1973. Report 73-322, USA.
[53] S.L. Qi, P. Zhang, R.Z. Wang, L.X. Xu, Flow boiling of liquid nitrogen in micro-tubes: part II–heat transfer characteristics and critical heat flux, Int. J. Heat Mass Transf. 50 (2007) 5017–5030.
[54] B. Zhang, Q. Li, Y. Wang, J. Zhang, P. Zhang, H. Jia, Experimental investigation of flow boiling heat transfer boundary of nitrogen in 1.2 mm vertical mini-channel, in: Proceedings of the International Heat Transfer Conference, Beijing, China 16, 2018, pp. 6861–6868.
[55] B.C. Zhang, Y.Wang Q.L.Li, J.Q. Zhang, J. Song, F.C. Zhuang, Experimental investigation of nitrogen flow boiling heat transfer in a single mini-channel, J. Zhejiang Univ. Sci. A 21 (2020) 147–166.
[56] K. Isao, I. Mamoru, Drift flux model for large diameter pipe and new correlation for pool void fraction, Int. J. Heat Mass Transf. 30 (1987) 1927–1939.
[57] C.L. Ong, J.R. Thome, Macro-to-microchannel transition in two-phase flow: part 1–two-phase flow patterns and film thickness measurements, Exp. Therm. Fluid Sci. 35 (2011) 37–47.
[58] H.K. Forster, N. Zuber, Dynamics of vapor bubbles and boiling heat transfer, AIChE J. 1 (1955) 531–535.
[59] M.G. Cooper, Saturation nucleate pool boiling - a simple correlation, in: Proceedings of the 1st UK National Conference on Heat Transfer, Leeds, England, 1984, pp. 785–793.
[60] D. Gorenflo, P. Sokol, Prediction method of pool boiling heat transfer with cryogenic liquids, Int. J. Refrig. 11 (1988) 315–320.
[61] X. Fang, Q. Wu, Y. Yuan, A general correlation for saturated flow boiling heat transfer in channels of various sizes and flow directions, Int. J. Heat Mass Transf. 107 (2017) 972–981.
[62] V. Gnielinski, Forced convection in ducts. Hemisphere Handbook of Heat Exchanger Design, Hemisphere Pub. Corp., Hemisphere, New York, 1990.
[63] D. Steiner, Wärmeübertragung Beim Sieden Gesättigter Flüssigkeiten, VDI Verlag Düsseldorf, 1988. Sect. Hbb, VDI Wärmeatlas.
[64] V.S. Devahdhanush, S. Lee, I. Mudawar, Experimental investigation of subcooled flow boiling in annuli with reference to thermal management of ultrafast electric vehicle charging cables, Int. J. Heat Mass Transf. 172 (2021) 121176.
[65] S. Lee, V.S. Devahdhanush, I. Mudawar, Investigation of subcooled and saturated boiling heat transfer mechanisms, instabilities, and transient flow regime maps for large length-to-diameter ratio micro-channel heat sinks, Int. J. Heat Mass Transf. 123 (2018) 172–191.
[66] A.P. Colburn, A method of correlating forced convection heat-transfer data and a comparison with fluid friction, Int. J. Heat Mass Transf. 7 (1964) 1359–1384.
[67] E.N. Sieder, G.E. Tate, Heat transfer and pressure drop of liquids in tubes, Ind. Eng. Chem. 28 (1936) 1429–1435.
[68] F.W. Dittus, L.M.K. Boelter, Heat transfer in automobile radiators of the tubular type, Int. Commun. Heat Mass Transf. 12 (1985) 3–22.
[69] M.G. Cooper, Heat flow rates in saturated nucleate pool boiling–a wide ranging examination using reduced properties, Adv. Heat Transf. 16 (1984) 157–239.
[70] V.P. Carey, Liquid-Vapor Phase-Change Phenomena: An Introduction to the Thermophysics of Vaporization and Condensation Processes in Heat Transfer Equipment, 3rd ed., Taylor and Francis, 2020.
[71] M. Blander, J.L. Katz, Bubble nucleation in liquids, AlChE J. 21 (1975) 833–848.
[72] R.W. Schrage, A Theoretical Study of Interphase Mass Transfer, Columbia University Press, New York, 1953.
[73] R. Cole, Boiling nucleation, Adv. Heat Transf. 10 (1974) 85–166.
[74] R.E. Sonntag, G.V. Wylen, Introduction to Thermodynamics–Classical and Statistical, 3rd ed., Wiley, New York, 1991.